Shape memory and mechanical properties of a Fe-Mn-Si-based shape memory alloy: Effect of crystallographic texture generated during additive manufacturing

I. Ferretto [a,b], D. Kim [c], W.J. Lee [d], E. Hosseini [a], N.M. della Ventura [a], A. Sharma [a], C. Sofras [e], J. Capek [e], E. Polatidis [e], C. Leinenbach [a,b,*]

[a] Empa, Swiss Federal Laboratories for Materials Science and Technology, 8600 Dübendorf-3602 Thun, Switzerland
[b] Laboratory for Photonic Materials and Characterization, École Polytechnique Fédérale de Lausanne, 1015 Lausanne, Switzerland
[c] Dongnam Division, Korea Institute of Industrial Technology, 50623 Yangsan, Republic of Korea
[d] School of Material Science and Engineering, Pusan National University 2, Busandaehak-ro 63beon-gil, Geumjeong-gu, Busan 46241, Republic of Korea
[e] Laboratory for Neutron Scattering and Imaging, Paul Scherrer Institute, PSI, 5232 Villigen, Switzerland

HIGHLIGHTS

- Assessment of correlation between grain orientation and martensite transformation in a Fe-based shape memory alloy;
- Modification of preferential texture by changing sample orientation during laser powder bed fusion process;
- Understanding the effect of crystallographic texture on deformation behavior, shape memory effect and mechanical properties.

GRAPHICAL ABSTRACT
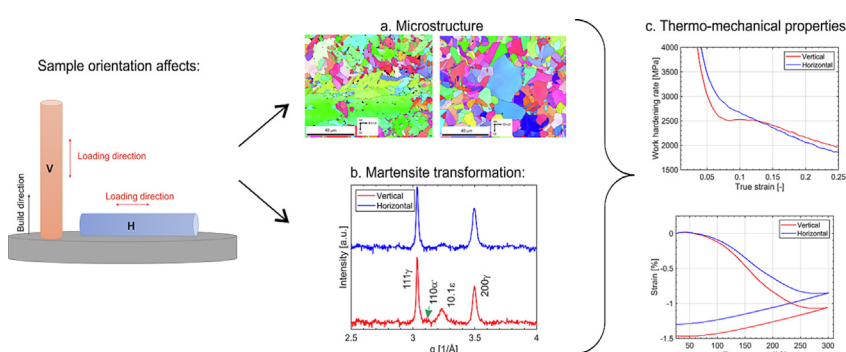
ARTICLE INFO

ABSTRACT

The fcc-$\gamma \rightarrow$ hcp-$\varepsilon \rightarrow$ bcc-α' martensitic transformation of a Fe-Mn-Si-based shape memory alloy fabricated by laser powder bed fusion (LPBF) is studied for the first time by in-situ neutron diffraction, in-situ high-resolution electron backscatter diffraction and digital image correlation during uniaxial tensile testing. The comparison between horizontal specimens (fabricated with no inclination on the build platform) and vertical specimens (fabricated with 90° inclination on the build platform) shows that sample orientation affects the deformation and transformation behavior of the material, considerably influencing alloy's shape memory and mechanical properties. The reason for the variation in the alloy's behavior is found in the distinct crystallographic texture generated during the LPBF process. In the vertical samples, the preferential $\langle 1\,1\,0 \rangle$ orientation of grains along the loading direction facilitates the martensitic transformation, resulting in enhanced shape memory properties and pronounced work hardening.

© 2023 The Author(s). Published by Elsevier Ltd. This is an open access article under the CC BY license (http://creativecommons.org/licenses/by/4.0/).

1. Introduction

Shape memory alloys (SMAs) are a class of materials that can recover their original shape after deformation. Thanks to their functionalities, SMAs are widely used in different engineering

fields, e.g. civil and structural engineering, aerospace, automotive, biomedical, and robotics. For example, SMAs are very suitable for fabricating actuators, sealers, and vibration dampers [1,2].

Commercially available shape memory alloys (SMAs) are mainly based on Nickel Titanium (NiTi) alloys. However, because of their high price and poor machinability [3], low cost Fe-Mn-Si-based SMAs have drawn much attention during the last two decades. Since the discovery of the shape memory properties on a Fe-30Mn-1Si single crystals [4], several Fe-Mn-Si alloy systems have been developed and investigated [5]. In all these studies, the formation of high concentration of stacking faults (SFs) within the austenite grain interior has been observed. Bergeon et al. investigated the formation mechanism of these SFs and their effect on the shape memory properties on a Fe-16Mn-5Si-9Cr-4Ni (wt.%) SMA [6]. Druker et al. showed that rolling the Fe–15Mn–5Si–9C r–5Ni (wt.%) alloy at 800 °C followed by annealing at 650 °C induces a high density of SFs that promotes the shape memory functionalities of the manufactured parts [7]. Extensive studies have also been performed on a Fe-15Mn-5Si-9Cr-5Ni fabricated by casting, annealing and final forging. Transmission electron microscopy (TEM) investigations show the presence of high density of overlapped SFs after solution treatment and water quenching [5,8,9]. The occurrence of SFs prior to and during deformation is based on the fact that Fe-Mn-Si-Cr-Ni SMAs have low stacking fault energy (SFE) [10]. For example, a SFE of 2.9 mJ/m^2 was calculated for the Fe-30.7Mn-6.5Si SMA [11], whereas for the Fe-30.3Mn-6.06Si SMA in [12] the SFE accounts for 7.8 mJ/m^2. In alloys with very low stacking fault energy (SFE) (<20 mJ/m^2), Shockley partial dislocations (SPDs) dissociate easily, causing the formation of a high density of SFs and their accumulation in deformation bands during loading [13,14]. The creation of SPDs on every second (1 1 1) layer of the fcc-γ austenitic matrix and the associated regular arrangement of SFs change the crystal structure into a hexagonal crystal structure, which is identified as hcp-ε martensite [15]. The transformation of fcc-γ austenite to hcp-ε martensite during loading and its reversion upon unloading, pseudo-elasticity (PE), and heating, shape memory effect (SME), are the mechanisms underlying the shape recovery of Fe-Mn-Si SMAs [16]. SFs thus play a dominant role in improving the shape memory properties of SMAs by acting as nucleation sites for the hcp-ε phase [17].

Several investigations have been performed in order to increase the alloys' shape memory properties. In one of the latest study on Fe-Mn-Si SMAs, compressive yield strength, fracture strength, as well as shape memory properties of the Fe–20Mn–6Si–8Cr–5Ni SMA could be improved by the addition of 0.5 wt% Ti [18]. The dissolution of Ti into the matrix lattice leads to solid solution strengthening and increases lattice microstrain in the alloy, providing a driving force for the fcc-γ → hcp-ε transformation. Recently, special focus has been placed on the optimization of the heat treatment conditions applied for Fe-Mn-Si SMAs containing C and carbide formers. For example, it has been observed that the application of two-step aging procedure facilitates precipitation nucleation and growth, allowing the fabrication of SMAs with high recovery stress (above 500 MPa) [19] and pronounced PE [20]. A significant variation in the recovery strain was also measured in the Fe-16.99Mn-5.59Si-9.28Cr-Ni5.67–0.12C SMA for different aging durations. The reduction of aging time from 180 min to 30 min leads to an increase in the recovery strain from 4.6 % to 5.4 % due to the formation of high density of precipitates, SFs and hcp-ε martensite [21].

At higher strains, the bcc-α' martensite forms inside the aforementioned deformation bands and at the intersections of hcp-ε laths. The volume fraction of bcc-α' increases with the strain [22]. The formation of bcc-α' martensite generally improves the strain hardening behavior of the material as this phase carries higher load than the austenite under external loading, acting as

reinforcing phase [23–25]. Additionally, bcc-α' martensite represents an efficient barrier for dislocation movement, reduces the mean free path of dislocations and thus causes an increase in the strain hardening rate [26,27]. Due to the fact that this phase does not contribute to the SME and hinders the back movement of SPDs and hcp-ε lamellae upon heating, shape memory properties decrease with the formation of bcc-α' martensite [28].

Additive manufacturing (AM) has attracted much attention in the past years as an innovative fabrication process that allows for high design freedom and short lead times [29]. 3D objects are fabricated by progressively adding thin layers of material based on a digital model. In the case of laser powder bed fusion (LPBF), a laser heat source is used to selectively fuse layers of spread powder, leading to the melting and solidifying of overlapping melt tracks. During the process, the fabricated component forms through a complex thermal history characterized by high thermal gradients, high heating and cooling rates, and cyclic re-heating, inducing significantly different microstructures compared to the conventional manufacturing process. High-Manganese (Mn) alloys exhibiting a transformation-induced plasticity effect (TRIP) or a twinning-induced plasticity effect (TWIP), or both, were recently successfully fabricated by AM [30,31]. The activation of the TRIP effect during deformation is the main mechanism responsible for the shape memory behavior of Fe-Mn-Si SMAs [32] and enhances their mechanical properties. Alloys showing TWIP and TRIP effects generally exhibit superior strength and plasticity in comparison with conventional steels, as the transformation of austenite to martensite and the formation of twins in the austenite grains raise the work-hardening rate and strengthen the material at the neck region [33]. The strength and ductility tradeoff can be overcome by fabrication of this class of steels by AM due to the generation of a graded microstructure with combinations of fine grains, directional grain architectures, high dislocation densities, solidification cell structures, solute segregations and metastable phases [30,31,34–41]. A strong anisotropic behavior in the tensile properties of these AM steels is, however, observed, which is mainly explained by the generation of pronounced crystallographic texture of the grains [31,40].

In the context of SMAs, Fe–17Mn–5Si–10Cr–4Ni SMA components showing pronounced shape memory properties were successfully manufactured by LPBF [42]. The achieved SME and PE significantly exceed those measured for the similar alloy Fe–17M n–5Si–10Cr–4Ni-1(V,C), but conventionally fabricated [43]. The reason for this improvement is also found in the specific microstructure developed during the LPBF process. The finer grains and the high density of SFs prior to loading facilitate the martensite transformation and its reversion [44]. The local variation in the chemical composition of the alloy due to evaporation and segregation phenomena also accounts for the differences in alloys' thermo-mechanical properties, as phase stability and SFE are affected [45].

Besides the possibility of manufacturing parts with complex geometries and enhanced performance, LPBF allows for a site-specific control of the microstructure in order to fabricate parts with tailored properties [46]. Changes in the processing parameters (heat input, scanning strategy [47–50]), build orientation [51] and part dimensions [52] result in variations in the final texture and microstructure as the local heat flux and the cooling rates are modified. The possibility of microstructure manipulation offered by LPBF process represents a significant advantage over conventional fabrication techniques, as mechanical and functional properties can be tailored according to the required performance of the parts. LPBF is thus highly beneficial for processing SMAs, whose functionalities strongly depend on sample microstructure. For example, significant variations in the alloy's strength and shape memory properties have been observed for the Fe–17Mn–5Si–10

Cr–4Ni-1(V,C) SMA simply by increasing the scan velocity (from 100 mm/s to 400 mm/s) [53]. The achieved mechanical and shape memory properties could be directly correlated to the changes in size, morphology and orientation of the grains introduced via modification of the processing parameters [53]. The rapid cooling and fast solidification experienced by the material during the process lead to the formation of bcc-δ ferrite as primary phase of solidification [54]. A dual phase bcc-δ (ferrite)/fcc-γ (austenite) microstructure thus characterizes the Fe–17Mn–5Si–10Cr–4Ni samples after LPBF [42]. The volume fraction and distribution of the two phases can be varied by adjusting the processing parameters as the thermal history experienced by the material affects the primary phase of solidification (bcc-δ or fcc-γ), as well as the extent of solid-state transformation of the primary bcc-δ to fcc-γ during the cooling stage [54]. Tensile samples made of Fe–17Mn–5Si–10Cr–4Ni SMA and showing different mechanical (yield strength, elongation to fracture and work hardening) and shape memory (SME and PE) properties could also be fabricated by changing the sample orientation on the build plate (Loading direction (LD) parallel to the build direction (BD) for the vertical samples and LD perpendicular to the BD for the horizontal samples) [42]. Specifically, a more pronounced SME was achieved in the samples whose LD is parallel to the BD. Kim et al. observed the same trend, where the PE and the SME of the same LPBF-manufactured alloy were measured by three-point bending tests [44]. However, a detailed investigation on the factors that give rise to this strong anisotropic behavior is still missing.

Understanding the microstructure changes associated with the LPBF processing parameters and their influence on the material's shape memory and mechanical proprieties represents the first step for a local tailoring of the microstructure of the LPBF-fabricated SMAs in order to achieve the desired thermo-mechanical and functional properties. Furthermore, for a better understanding of the mechanical behavior of the material, the complex interaction between preexisting nucleation sites, plasticity, formation and evolution of microstructure (e.g. SFs, twins, texture, etc.), and phase transformations have to be considered. In this regard, in-situ experiments during deformation allow for characterization of the phase transformation behavior responsible for the PE and SME in the different microstructures developed during LPBF, providing a coupling between bulk mechanical behavior and microstructure evolution. Additionally, with neutron diffraction it is possible to follow the evolution of the macroscopic and microscopic lattice strains and the load partitioning between grain families/phases, which are classified with respect to their orientation, and the scattering vector.

The deformation behavior of conventionally produced Fe-Mn-Si SMAs has been previously studied [55–57]. However, AM-processed materials are expected to exhibit significantly different mechanical behavior due to the unique microstructures generated during the AM process. Furthermore, among all these studies, the martensitic transformation has been mainly examined on a macroscopic scale. The deformation behavior of the material in the microscale is also an important aspect of optimizing the PE and SME effects, as microstructural and deformation heterogeneity in terms of amount, size and morphology of transformed martensite among differently oriented grains can be detected. Capable methods for studying deformation at this scale are high-resolution electron backscatter diffraction (EBSD) and digital image correlation (DIC) of high magnification images acquired by scanning electron microscope (SEM). When applied in-situ, the evolution of martensite transformation with the deformation can be followed and locally tracked during loading. Therefore, in the present study, the martensitic transformation is investigated in Fe–17Mn–5Si–10Cr–4Ni SMA samples fabricated by LPBF using in-situ neutron diffraction and in-situ EBSD and DIC. This work describes the effect of sample orientation on texture formation, phase transformations and lattice strain variation during deformation. The detailed view of the microstructure evolution during loading is directly correlated with the macroscopic thermo-mechanical properties of the LPBF-fabricated samples, shedding light on the main mechanisms governing the alloy's response. The dependence of the martensitic transformation on austenite grain orientation is also discussed to explain the effect of sample texture on martensite formation, shape memory, and mechanical properties.

2. Materials and methods

2.1. Powder

The material investigated in this work is the Fe-Mn-Si-based SMA already investigated in the previous studies [42,44,58], whose composition, as provided by the powder supplier, is given in Table 1. The powder was produced by gas atomization in Argon atmosphere (Metal Player Co., ltd., Republic of Korea) and is characterized by spherical particles with a d_{50} of 29.7 μm and a size distribution between 10 and 50 μm.

2.2. Sample fabrication

The investigated samples were fabricated by LPBF with a Sisma MySint 100 LPBF machine (Sisma S.p.A., Italy) in an argon environment to keep the oxygen content below 0.1 %. The machine is equipped with a 1070 nm fiber laser, with a Gaussian intensity distribution and a spot size of 55 μm.

For the sample fabrication, the LPBF machine operated with a laser power of 175 W and a scanning speed of 300 mm/s. The hatch spacing was set to 0.1 mm and the layer thickness to 0.03 mm. A bidirectional scanning strategy without border contour was used. A scanning rotation of 90° was applied between subsequent layers. The selection of processing parameters was based on the previous investigation [42], where it was found that a high volumetric energy density (194.44 J/mm³) has to be applied in order to avoid cracking, less amount of fusion defects and fabricate dense parts. As shown in Fig. 1-a, cylindrical bars with different build orientations with respect to the build plate were fabricated. The vertical bars have the main axis parallel to the BD, and the horizontal ones have an axis perpendicular to the BD. All bars were annealed at 800 °C for 2 h to dissolve residual bcc-δ (ferrite) [42,44]. Round specimens with a gauge length of 25 mm and a diameter of 6 mm were machined from the heat-treated cylindrical bars (Fig. 1-a). In this way, tensile samples with different orientations of the LD with respect to the BD (parallel for the vertical samples and perpendicular for the horizontal samples) were obtained.

Cylindrical tensile samples were fabricated for the neutron investigations (shown in Fig. 1-a), whereas flat tensile samples were used for the in-situ EBSD and DIC investigations [59]. The flat tensile specimens with the geometry shown in Fig. 1-b were produced by electro discharge machining (EDM). Samples were machined from a horizontal block as with this orientation no preferential texture is generated [42]. In this way, several grains with different orientations could be investigated. The obtained tensile samples have the LD perpendicular to the BD. For the thermomechanical characterizations, samples from both vertical and horizontal building orientations were used.

Table 1
Chemical composition of the Fe-based SMA powder.

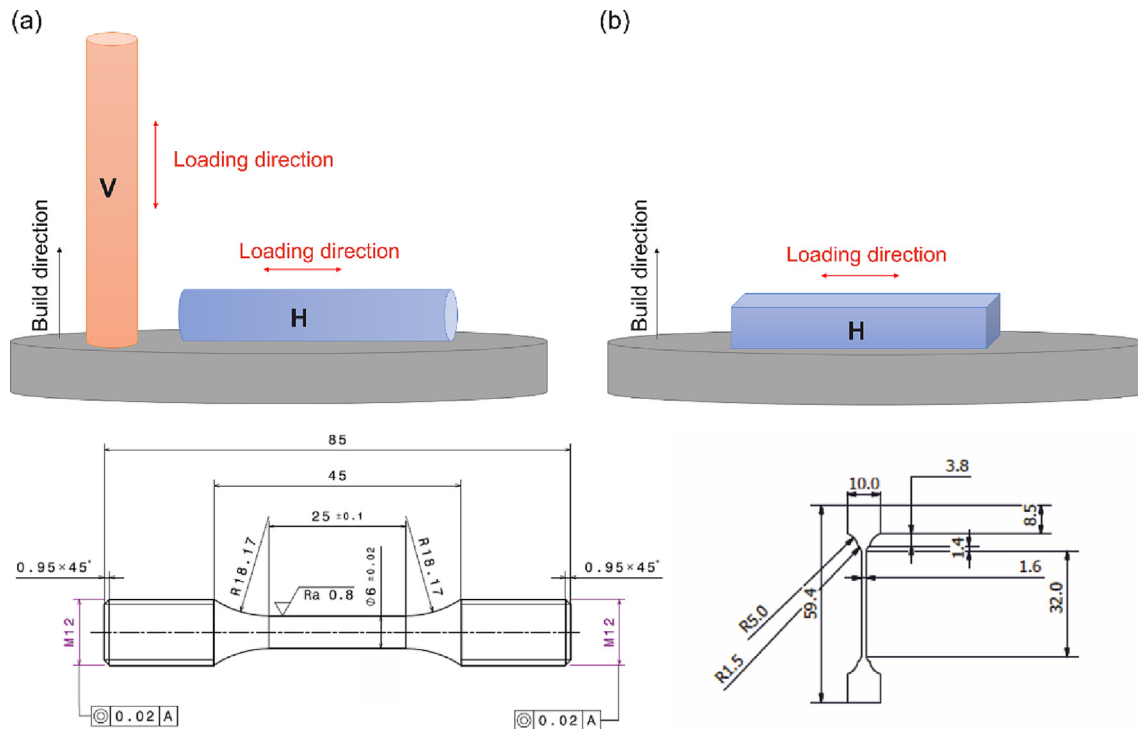| Fe (wt. %)	Mn (wt. %)	Cr (wt. %)	Si (wt. %)	Ni (wt. %)
bal.	17.3	9.9	5.1	4.0

Fig. 1. Orientation of the cylindrical samples (V vertical, H horizontal) with respect to the BD and related technical drawing (a); orientation of the flat tensile samples and related technical drawing (b);

2.3. Sample characterization

2.3.1. Texture and microstructure

Texture and microstructure were investigated for the horizontal and vertical samples before and after the neutron diffraction tests. A cross-section of the gripping part and one within the gauge length of the samples were analyzed in order to investigate the microstructure in the un-deformed state and after the deformed state (at 10 % engineering strain), respectively. The surfaces were mechanically ground with 600, 1200, 2500 and 4000 grit SiC paper and electrochemically polished for 10 s with a 16:3:1 (by volume) ethanol, glycerol and perchloric acid solution at 50 V for 10 s. The EBSD was performed using a field emission gun scanning electron microscope (FEG SEM) Zeiss ULTRA 55 equipped with EDAX Hikari Camera operated at 20 kV in high current mode and with a 120 μm aperture. The acquired EBSD raw data were post processed using the EDAX OIM Analysis 7.3 software.

The amount of magnetic phases in the clamping part and in the gauge length of the samples was (semi)quantified by magnetic induction measurements using the FMP30C [60].

Transmission electron microscopy (TEM) analysis was performed with a Thermofisher Titan Themiz Z, using an acceleration voltage of 300 kV. The TEM specimen was prepared from a flat un-deformed sample by focused ion beam milling (Thermofisher Helios G4 UC).

2.3.2. In-situ neutron diffraction during tensile test

In-situ neutron diffraction tests were performed on the cylindrical tensile samples shown in Fig. 1-a and with the two different orientations of the LD (vertical and horizontal samples). For the tensile tests, the uniaxial deformation stress rig with 30 kN load capacity of the time-of-flight (TOF) strain scanner POLDI at the SINQ Swiss spallation source (Paul Scherrer Institute, Villigen, Switzerland) was used. A clip-on extensometer of 25 mm was mounted on the samples to measure the macroscopic strain. The

samples were strained with a strain rate of 0.4x10^{-3}/s until a maximum strain of 10 % and then unloaded.

Neutron diffraction measurements were undertaken during the tensile test at predefined forces (elastic regime) and strains (plastic regime) by interrupting the loading and keeping the displacement fixed. For every interruption (12 interruptions during loading and 4 during unloading), the displacement was kept constant and the neutron acquisition was performed after allowing 180 s of relaxation time. The neutron diffraction acquisition time was defined by a monitor counter before the sample and ranged from about 20 min per point in the elastic regime to 110 min in the plastic regime. The acquisition time was increased for the measurements in the plastic regime to detect the weak hcp-ε peaks that have a lower signal-to-noise ratio compared to the initial fully austenitic material. The incident neutron beam is characterized by wavelength ranging between 1.1 and 5 Å. The POLDI instrument is equipped with a detector bank positioned at an angle of 90° with respect to the incident beam. The samples were mounted in a way that the LD of the cylindrical sample was parallel to the scattering vector and a 3.8 × 3.8 × 3.8 mm^3 gauge volume was defined by a pair of diaphragms and a radial collimator. In this way, the hkl lattice planes with their < hkl > direction parallel to the LD fulfill the Bragg condition (axial configuration). A second set of samples was mounted with the LD perpendicular to the scattering vector (transverse configuration). In this configuration, the gauge volume was 10 × 3.8 × 3.8 mm^3, which improved the counting statistics due to the larger probed volume. Fig. A1 in Appendix A shows a schematic detailing the two different configurations, axial and transverse, used for neutron diffraction measurements.

The diffraction peaks were fitted with the single-peak fitting routine available in the open source software Mantid [61]. Phase transformation, load partitioning and lattice strains were investigated by following the evolution of peak position and integrated intensity of both the austenite and martensite diffraction peaks of the recorded patterns. In particular, the fcc-γ peaks 220, 111,

200 and 311 and the hcp-ε peaks 10.1, 10.3, 20.1 and 20.3 were analyzed in terms of variation of the integrated intensity with the applied strain. The lattice strains for a lattice plane family at every stress level were also calculated as:

$$\varepsilon_{hkl} = \frac{d_{hkl} - d_{0hkl}}{d_{0hkl}} \tag{1}$$

where the d_{hkl} is the lattice spacing of the hkl family of planes in the loaded stated and d_{0hkl} before loading.

2.3.3. In-situ EBSD and in-situ DIC during tensile test

In-situ EBSD mapping was carried out on a flat sample to investigate the phase transformations during loading for different grain orientations. A Kammrath and Weiss tensile-compression module with a 5 kN load cell was installed inside the chamber of the FEG SEM Zeiss ULTRA 55. The EBSD mapping was always performed in the same area at different deformation stages (0, 1, 2, 4 % strain) by interrupting the loading and keeping the displacement fixed. The displacement rate was 0.002 mm/s. EBSD maps were acquired with a step size of 80 nm and an aperture size of 120 μm.

In-situ high-resolution DIC analysis was also performed to investigate the martensite transformation during deformation with the same tensile rig and SEM used for the in-situ EBSD analysis. All the analyses were performed in a polished area of the cross-section of a flat sample. After polishing, a thin gold film was deposited. The method described in [59] was applied in order to get images for DIC. The in-lens detector of the SEM was used. A working distance of 7.5 mm, an acceleration voltage of 3 kV and an aperture size of 20 mm were selected to minimize topographic contrast and obtain a sufficiently good signal/noise ratio. SEM images were taken in four different positions of the sample for every strain condition (0 %, 2 %, 4 % strain) and then overlapped. The analysis was performed using the Ncorr open-source 2D-DIC software for MATLAB [62]. The strain along the LD, ε_{xx}, the in-plane transverse direction, ε_{yy}, and the in-plane shear strain, ε_{xy}, were used to calculate the effective strain:

$$\varepsilon_{eff} = \sqrt{\left(\frac{\varepsilon_{xx} - \varepsilon_{yy}}{2}\right)^2 + \varepsilon_{xy}^2} \tag{2}$$

Thus the surface strain maps for 2 % and 4 % deformation are presented as maximum shear strain, effective strain ε_{eff}, as explained in [59,63].

2.3.4. Thermo-mechanical characterization

The stress–strain behavior of vertical and horizontal flat dog-bone samples was determined by strain-controlled tensile tests until failure in a Zwick/Roell Z020 tensile testing machine at room temperature (RT). It is known that the nonlinear stress–strain observed for Fe-Mn-Si alloys is due to martensite transformation, plastic flow, or a combination of both. According to Lee et al., the 0.1 % yield stress is bettersuited for estimating the stress onset for the martensite transformation than the 0.2 % yield stress [64,65]. For this reason, both the yield stress 0.1 % and 0.2 % were calculated in this work and defined as $\sigma_{0.1}$ and $\sigma_{0.2}$, respectively. Ultimate tensile stress (UTS) and elongation to fracture were obtained from the engineering stress–strain curves. The evolution of the work hardening rate was also calculated from the true stress–strain curves of both samples.

The recovery strain, ε_{rec}, after deformation and heating was characterized for the two sample orientations. The strain evolution was recorded by a side-entry extensometer with a datum leg spacing of 10 mm. The tensile samples were pre-strained to 4 % at RT and at a strain rate of 0.01 %/s, followed by unloading. After pre-straining, one end of the sample was released, and the extensometer was reset to zero strain. The sample was heated up to 300 °C

and cooled down to RT at a rate of 2 °C/min. The temperature was kept constant for 30 min when the maximum temperature (i.e. 300 °C) and RT were reached to ensure a homogenous temperature distribution within the samples. The final strain measured by the extensometer at the end of the thermal cycle was recorded as ε_{rec}. The same procedure was performed for a pre-strain of 10 %, followed by heating to 300 °C.

3. Results

3.1. Microstructure and texture

3.1.1. Microstructure and texture before deformation

Fig. 2-a,b shows the EBSD analysis for the vertical and horizontal samples prior to the deformation. According to the EBSD maps with inverse pole figures (IPF) color triangles, different textures of the austenite phase can be generated along the LD by varying the sample orientation with the BD. Specifically, a weak/random crystallographic texture develops along the LD of the horizontal sample, whereas the vertical sample shows grains with a preferred ⟨110⟩ orientation along the LD. The scan area has been selected to cover a sufficient number of grains to get statistically accurate texture information. The EBSD based texture analysis is complemented by the neutron diffraction experiments, which have been performed on the same samples to achieve even higher statistical accuracy (section 3.3.1). The variation in the texture of the samples along the LD is related to the fact that grains preferentially grow with the ⟨110⟩ direction aligned towards the BD, which corresponds to the LD of the vertical sample. The preferential ⟨110⟩ texture along the BD is ascribed to the solid-state transformation bcc-δ → fcc-γ that occurs through the intrinsic heat treatment generated during the layer-wise deposition [54]. Some elongated grains parallel to the LD of the vertical sample are observed (Fig. 2-a,b). This is in agreement with the preferred solidification in the direction of the heat flow. As most of the induced heat is usually directed towards the substrate, most grains show a high aspect ratio, with the largest dimension in the BD, which corresponds to the LD of the vertical sample.

Similar grain sizes are achieved in the two samples, with slightly finer grains in the vertical sample (average diameter of 6. 16 ± 2.89 μm) compared to the horizontal one (average diameter of 6.72 ± 3.18 μm).

The grain size histogram for both samples is reported in Fig. A2 of Appendix A.

The TEM analysis before deformation shows a high concentration of SFs (indicated by red arrowheads) prior to loading (Fig. 2-c,d), as already pointed out in [54] for the same alloy. The formation of SFs in LPBF-manufactured parts has been observed in several austenitic steels [34,35,37]. The rapid solidification experienced by the material during fabrication causes the formation of fine cellular structures. A high density of tangled dislocations with a high tendency to dissociate normally characterizes the walls of these structures, leading to the formation of wide SFs [66]. Dense SF arrays in the present alloy are also introduced at the bcc-δ/fcc-γ interface during the afore-mentioned shear-induced solid-state transformation bcc-δ → fcc-γ [54].

3.1.2. Microstructure and texture after deformation

EBSD analysis was performed on the gauge length of the cylindrical samples after neutron diffraction investigations, i.e., after 10 % engineering strain. The EBSD maps with phase coloring (Fig. 3-a,b) reveal that, especially for the vertical sample, a high volume of hcp-ε martensite forms in the austenite grains upon loading. The absolute values of phase fractions obtained from the EBSD analysis are more approximate qualitative estimations of
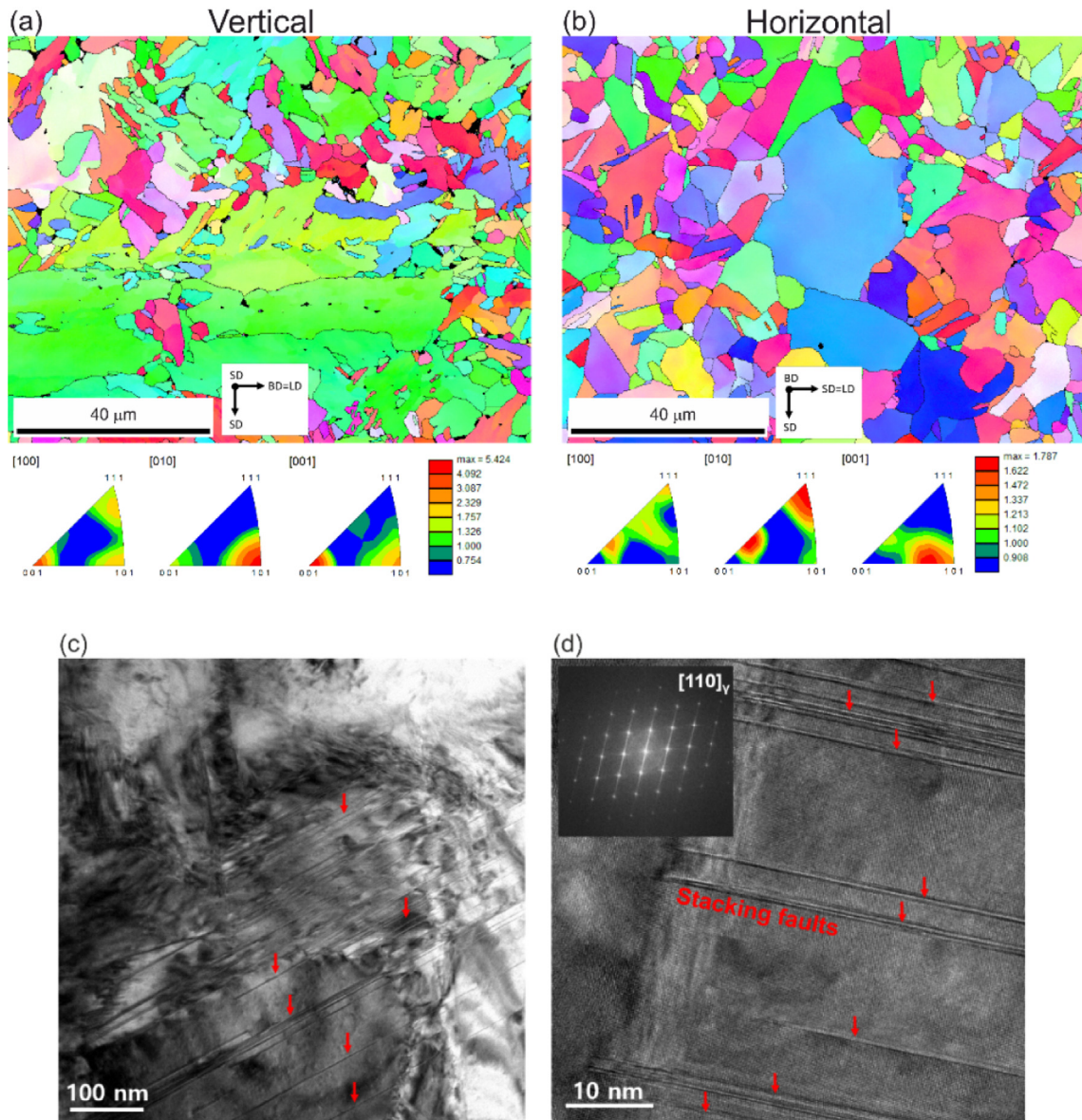
Fig. 2. EBSD maps with IPF coloring related to the LD and IPFs of the vertical sample (a) and of the horizontal sample (b); TEM images showing the presence of SFs prior to deformation in the fabricated samples (c,d);

the phase concentration as the investigated areas are rather small and the grain statistics relatively low. However, from the comparison of the two EBSD maps, it is clear that the amount of hcp-ε is higher in the vertical sample than in the horizontal sample (phase fractions of hcp-ε are 34 % and 26 %, respectively). Martensite (hcp-ε) forms with a texture along the LD and follows the Shoji–Nishyama (S—N) orientation relationship [67], where {111}γ // {0001}ε, ⟨110⟩γ // ⟨1 2̄ 1̄ 0⟩ε (Fig. 3-c,d,e,f).

The high-resolution EBSD map with phase coloring performed in a smaller area on the gauge length of the vertical sample shows the formation of bcc phase that is identified as residual bcc-δ ferrite, which did not completely dissolve after annealing, and as bcc-α′ martensite (Fig. 3-e). According to the semi-quantification of the amount of bcc phase by magnetic induction measurement, the concentration of bcc phase on the gauge length of the samples (4.54 % ±0.08 % for the vertical sample, 1.69 %±0.07 % for the horizontal sample) is higher compared to the clamping part (0.31 % ±0.09 % and 0.28 % ±0.07 %), indicating that most of the bcc phase in the deformed section is deformation-induced bcc-α′. This can be

additionally confirmed by the fact the bcc-α′ forms at the expense of hcp-ε, following the orientation relationship {0002}ε // {011}α′, ⟨2̄ 1̄ 1̄ 0⟩ε // ⟨11 1̄⟩α′ (Fig. 3-e,g) [68], which is indicative of a sequence of deformation-induced transformation.

3.2. Stress–strain and shape memory response

3.2.1. Stress–strain response

Fig. 4-a shows the engineering stress–strain (σ-ε) response of the vertical and horizontal samples until the failure. The vertical sample has a lower yield ($\sigma_{0.1}$ 223.9 ± 10 MPa and $\sigma_{0.2}$ 258.6 ± 5.9 MPa) than the horizontal sample ($\sigma_{0.1}$ 239 ± 5.2 MPa and $\sigma_{0.2}$ 297 ± 6.5 MPa). For both samples, the engineering σ-ε curve deviates from a linear trend at stresses well below $\sigma_{0.1}$. An earlier deviation is already observed for the vertical sample at an engineering stress of approximately 140 MPa (Fig. 4-b). A more gradual deviation is observed for the horizontal sample at higher engineering stress, around ∼ 200 MPa.
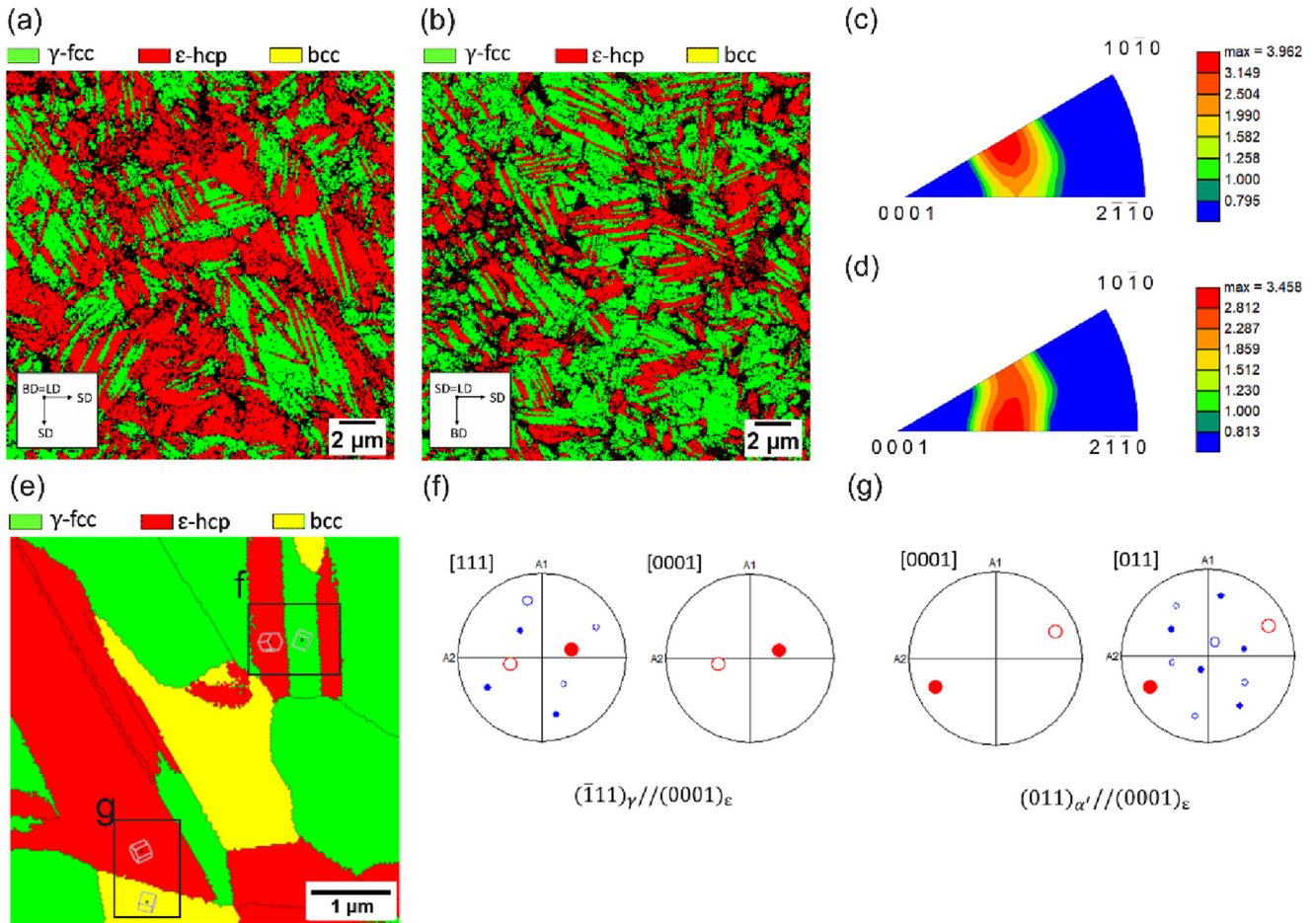
Fig. 3. EBSD maps with phase coloring from the gauge length of the vertical (a) and horizontal (b) samples after 10% pre-straining; IPFs with respect to the LD for the hcp-ε in the vertical (c) and horizontal (d) samples; high magnification EBSD map with phase coloring for the gauge length of the vertical sample, showing the formation of bcc-α' martensite (e); pole figures of selected grains, showing the orientation relationship between fcc-γ and hcp-ε (f), and between hcp-ε and bcc-α'(g);
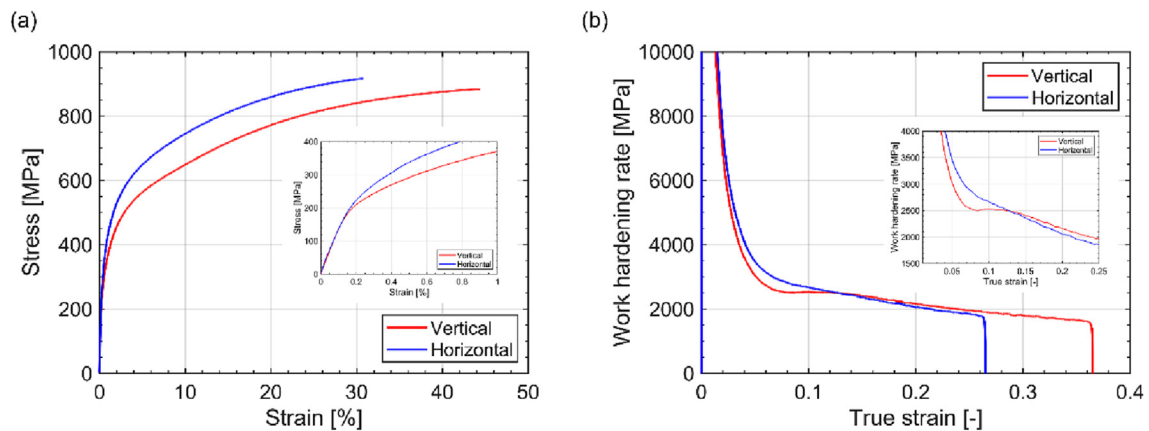

Fig. 4. Engineering stress–strain curves of the vertical and horizontal samples (a-b); work hardening rate curves as a function of the true strain for the vertical and horizontal samples (c-d);

Regarding the UTS, the same trend was already reported in the previous study [42], with the vertical sample showing lower strength (UTS of 876.8 ± 8.6 MPa) but higher elongation to fracture (43.3 ± 6.2 %) compared to the horizontal sample (UTS of 928.5 ± 12.2 MPa and elongation to fracture of 34.9 ± 1.1 %)). The work hardening rate is calculated from the true stress and true strain and reported in Fig. 4-b. The work hardening rate is not significantly different; however, it appears to slightly increase above

8 % applied true strain for the vertical sample. Contrary to the vertical sample, the work hardening rate of the horizontal sample continues to decrease until final failure without any increase.

3.2.2. Shape memory response – Recovery strain
Fig. 5-a shows the recovery strain of the cylindrical samples after 4 % pre-straining, followed by heating up to 300 °C and subsequently cooling to RT.
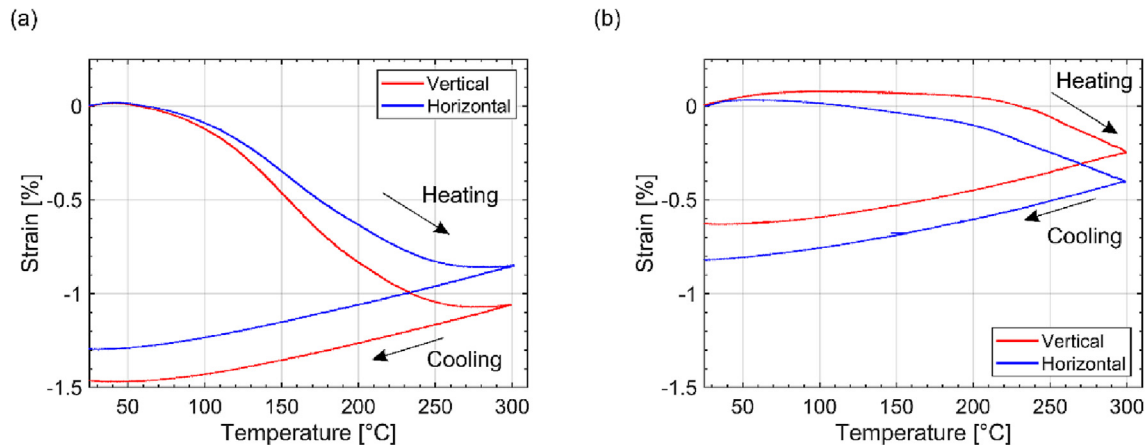
(a)　　　　　　　　　　　　　　　　(b)

Fig. 5. Recovery strain as a function of temperature after 4 % (a) and 10 % (b) pre-straining and annealing at 300 °C for the vertical and horizontal samples;

The evolution of the strain recovery curve is defined by a combination of sample expansion (associated with the material's thermal expansion) and sample contraction (associated with the phase transformation reversion hcp-ε → fcc-γ) during heating and by thermal contraction during cooling. For 4 % pre-strain (Fig. 5-a), a pronounced sample contraction is observed upon heating, indicating a large amount of reverse martensitic transformation. The recovered strain is higher in the vertical sample than in the horizontal one at 300 °C (1.02 % and 0.85 %, respectively) and after cooling to RT (1.47 % compared to 1.29 %, respectively). For both samples, the contraction starts at around 45 °C, but it proceeds faster for the former, suggesting a more readily and pronounced back transformation.

When the samples are pre-strained up to 10 % (Fig. 5-b), the recovery strain reduces to almost half the values observed for the 4 %-strained samples. Considering the influence of the sample orientation, an opposite trend than in the case of pre-straining to 4 % is observed. The final recovery strain achieved at RT for the horizontal sample is 25 % higher than for the vertical one. For the vertical sample, the recovery strain curve is rather flat up to 200 °C, indicating that up to this temperature, the SME is active and balances the thermal expansion effect, but is not enough to exceed it. For the horizontal sample, phase transformation becomes predominant and overcomes the effect of thermal expansion at temperatures below 100 °C, indicating a more pronounced SME compared to the vertical sample.

3.3. In-situ neutron diffraction

3.3.1. Evolution of peak intensities

Fig. 6-a shows the diffraction patterns for the un-deformed state for the horizontal and vertical samples. A comparison of the initial intensity of the austenite peaks before loading validates the different textures generated with the variation of the sample orientation with respect to the BD already observed by EBSD analysis. Grains show a preferential alignment of the ⟨110⟩ direction along the LD of the vertical sample (i.e., the {220} lattice plane families are perpendicular to the LD), whereas no preferential orientation is observed for the horizontal sample.

The evolution of the diffraction patterns in the selected q-values of 2.8–3.6 Å^{-1} obtained using the axial configuration are exemplarily reported for the vertical sample after 0, 4, 8,10 % strain, as well as unloaded after 10 % strain (Fig. 6-b). A pronounced intensity reduction of the austenite 111 and 200 peaks is observed at 4 %. By increasing the strain up to 8 and 10 %, peak intensity still reduces, but the reduction is less pronounced. Upon unloading,

an intensity increase is observed. With increasing strain, new peaks appear which are associated with the formation of hcp-ε phase (martensite). During deformation, the hcp-ε martensite peaks experience an opposite trend (intensity increase during loading, intensity decrease during unloading) compared to the austenite peaks, confirming the onset of the fcc-γ → hcp-ε transformation upon loading and a partial reversion hcp-ε → fcc-γ during unloading. Although a decrease of the fcc-γ peak intensity is observed at very low strain (<1%), the hcp-ε peaks can be identified only at higher strain. This can be explained by the lower symmetry of the hcp crystal structure, which results in more diffraction peaks than cubic crystal structures, and the rather low initial fraction of hcp-ε. The low intensity of the hcp-ε diffraction peaks and their overlapping with the fcc-γ peaks render the identification of the hcp-ε rather complex at low strain, when the fraction of martensite is low.

Fig. 6-c,d shows the evolution of the integrated intensity of the austenite peaks, i.e. the peak intensity normalized by the initial intensity at 0 % strain, as a function of the macroscopic engineering strain for the {111}, {220}, {200} and {311} grain families and for the two sample orientations. The integrated intensity of most of the analyzed austenite peaks ({111}, {220}, {200}) decreases with increasing strain. According to previous neutron diffraction investigations on fcc metals and alloys [69], the diffraction intensity of the 111 and 200 diffraction peaks increases with the strain in the LD due to the deformation texture development induced by dislocation-based plasticity. The 111 peak normally shows the largest increase in intensity in the LD due to deformation texture. The decrease in the integrated intensity of the 111 peak observed here is thus an indication of the dominance of the phase transformation of austenite over texture development. Based on these observations, it can be assumed that, for the investigated alloy, martensite formation is the dominant deformation mode and superimposes the effect of dislocation slip already at the beginning of deformation.

As plastic deformation proceeds, the austenite diffraction peaks exhibit distinctive variations in their intensities. Very similar trends are observed if the same grain families in the vertical and in the horizontal samples are compared. The intensity reduction occurs in different amounts and with a different rate for differently oriented grains. A particular behavior is observed for the 311 peak, whose intensity remains almost constant during loading, presumably because of a balance between transformation and deformation texture development. A pronounced reduction in intensity for the 220 peak, i.e. decrease of almost 75 %, is observed. Such strong reduction is a result of both decrease by the formation of
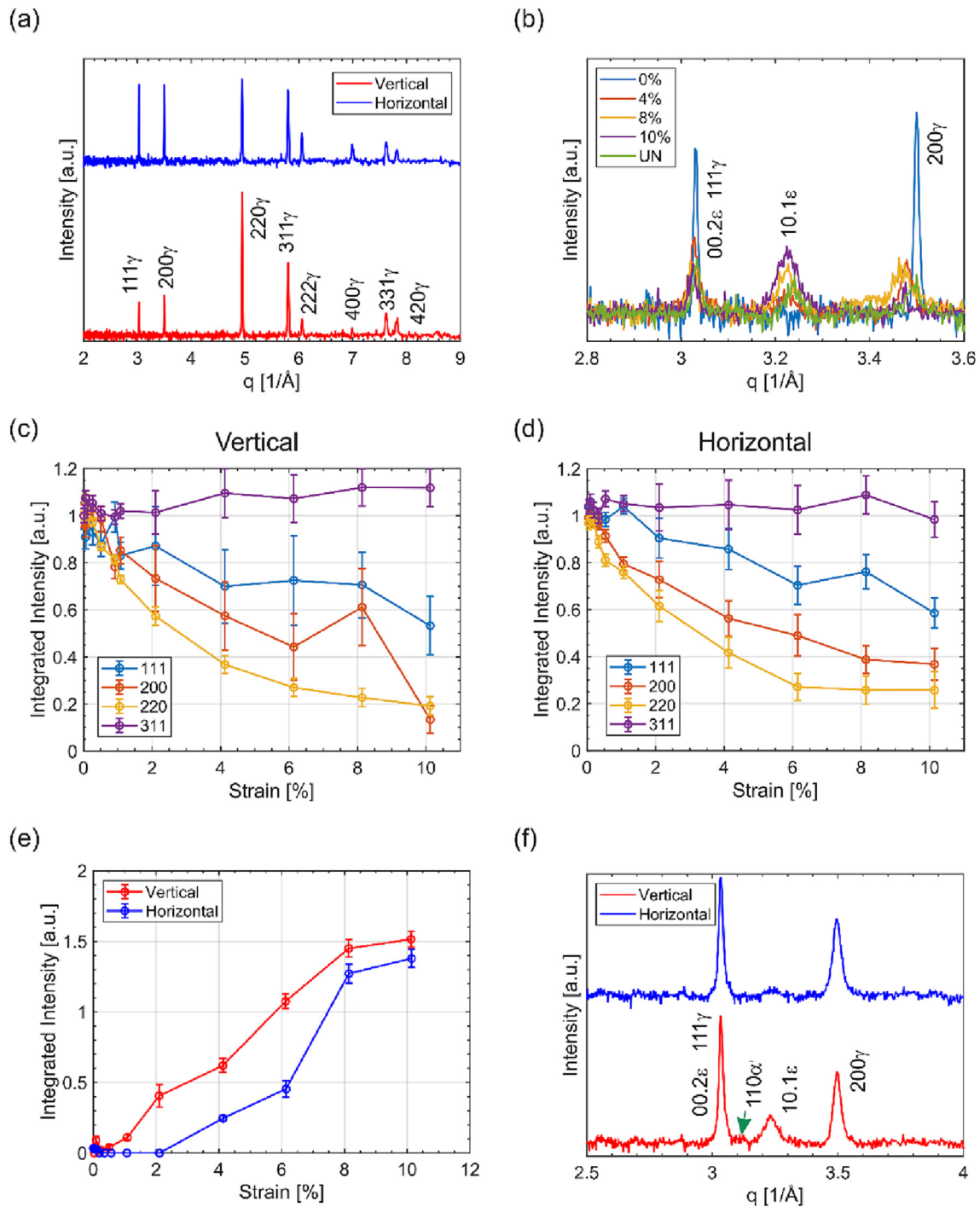
Fig. 6. Diffraction patterns at the initial stage (un-deformed) for the two different sample orientations (a); diffraction peak evolution with the applied engineering strain for the vertical sample in the selected q-range 2.9–3.6 Å-1 (axial configuration) (b); integrated intensity evolution with the applied engineering strain of the austenite peaks of the vertical (c) and horizontal (d) samples (axial configuration); summed integrated intensity evolution with the applied engineering strain of the 10.1ε, 10.3ε, 20.1ε and 20.3ε martensite peaks of the vertical and horizontal samples (transverse configuration) (e); diffraction patterns at 4 % engineering strain of the vertical and horizontal samples (transverse configuration) (f);

deformation texture and phase transformation. The intensity of the 111 and 200 peaks also reduces due to transformation despite the effect of deformation texture that in the absence of transformation would exhibit an increase in the diffraction intensity.

The evolution of the 10.1ε, 10.3ε, 20.1ε and 20.3ε martensite peaks of the two samples is analyzed from the neutron diffraction patterns. For this analysis, the transverse configuration was used due to better counting statistics and better signal-to-noise ratio.

It is also important to note here that strain-induced martensite exhibits less strong crystallographic texture in the transverse direction. In Fig. 6-e, the sum of the integrated intensity of the four hcp-ε martensite peaks normalized by the monitor counting (see experimental) is reported as a function of the applied engineering strain for the vertical and horizontal samples. By considering multiple peaks, the effect of the possibly mild texture difference of martensite between the two samples is negligible and the inte-

grated intensity can be correlated qualitatively with the amount of martensite. During loading, the sum of the integrated intensities is higher for the vertical sample compared to the horizontal one, especially at the beginning of the deformation. The integrated intensities of the martensite peaks can be already measured at strain < 2 % for the vertical sample, whereas the martensite peaks in the horizontal sample are too broad and with too low intensity to be fitted (Fig. 6-e), indicating an earlier and more pronounced phase transformation at the beginning of the deformation in the vertical sample (Fig. A3 of Appendix A). Only at 4 %, some martensite peaks can be detected and fitted. Peaks are still very broad and with a low intensity (Fig. 6-f).

Peaks corresponding to the bcc-α' phase are also identified in the diffraction patterns. At 4 % strain, a relatively wide peak with low intensity is observed in the diffraction pattern of the vertical sample at q of 3.098 Å^{-1} (transverse configuration), which corresponds to the 110α' peak (Fig. 6-f). The peak intensities of the bcc-α' phase slightly increase with strain up to 10 % (Fig. A5-a,b of Appendix A), becoming well visible at a strain of 8 % (Fig. A4-a,b of Appendix A). The diffraction pattern of the horizontal sample also shows the 110α' peak, but only at 10 % strain (Fig. A5-c,d of Appendix A). At 8 % (Fig. A4-c,d) and lower strain, the amount of bcc-α' is too low to be detected by neutron diffraction. Compared to the vertical sample, the peak intensity is lower and the peak is rather broad. The high asymmetry of the diffraction peak at q ~ 5.3 Å^{-1} at 8 and 10 % strain of the vertical sample shown in Fig. A4-b and Fig. A5-b of Appendix A is assumed to result from the peak overlap of the 211α' and 10.3ε peaks, confirming the formation of bcc-α' during loading.

3.3.2. Evolution of lattice strains

Fig. 7-a,b reports the elastic strain for the 4 different grain families of fcc-γ {111}, {200}, {220} and {311} (ε_{111}, ε_{200}, ε_{220}, ε_{311}) for both the vertical and horizontal samples with respect to applied macroscopic engineering stress.

The lattice strains reveal a monotonic increasing trend as a function of stress in the LD. In the first stage, all grain families deform elastically, and the lattice strains increase linearly. The linearity changes with grain orientation due to elastic anisotropy, showing the highest specific modulus for the ⟨111⟩ direction and the lowest for the ⟨200⟩, as already observed for most of the fcc materials [70]. In the second stage, the curves deviate from linearity. For the {220} grain family of the vertical sample, the slope of the lattice strain curve reduces and grains carry less elastic strain than what would be expected from the extrapolation of the linear elastic behavior, implying that they undergo plastic deformation. Similar behavior is observed for the {111}, but the decrease in the lattice strains is less pronounced and occurs at higher stress. The load that is not carried by the {220} and {111} grains appears to be transferred to the {200} grains, which develop large elastic strain. This observation agrees well with previous diffraction studies where the {200} grains continue to accumulate significant load at an increased rate [55,56,71,72].

The divergence from the linear behavior is similar for the grains in the horizontal sample, with {111} and {220} grains exhibiting plasticity and shedding their load to the {200} grains. Fig. 7-c,d compares the evolution of the lattice strains for the {220} and {200} grains as a function of the macroscopically applied engineering stress for the vertical and horizontal samples. Contrary to the
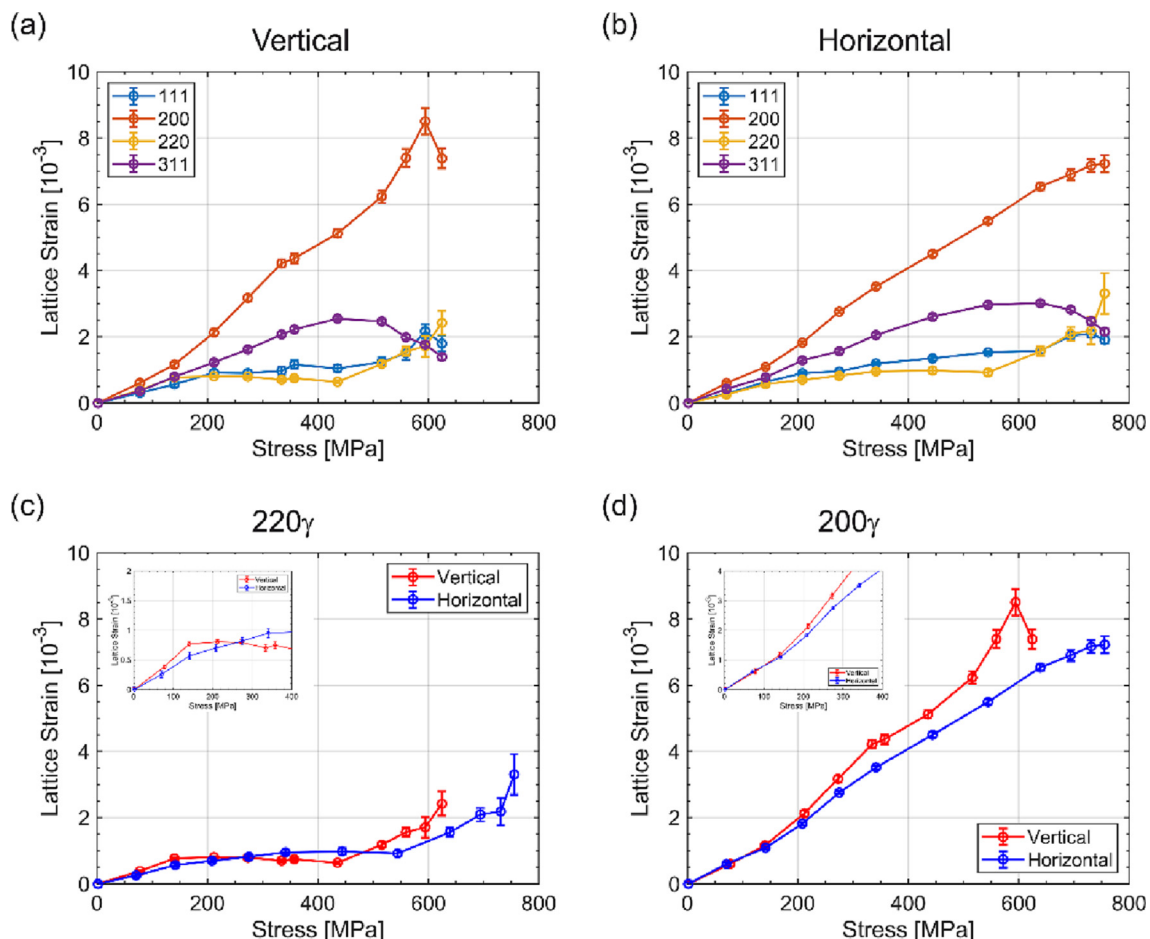

Fig. 7. Lattice strain evolution with the applied engineering stress of the austenite grain families of the vertical (a) and horizontal samples (b); comparison of the lattice strain evolution with the applied engineering stress of the {220} (c) and {200} (d) austenite grains of the vertical and horizontal samples (axial configuration);

vertical one, in the horizontal sample the {220} grains do not deform fully plastically post yielding but undergo a slight increase in the elastic strain up to 400 MPa. This indicates that that the {220} grain family in the horizontal sample still carries some elastic strain post-yielding, resulting in inferior load transfer to the {200} grains when compared to the same grain family of the vertical sample (Fig. 7-d).

At a stress of 335 MPa, the increase rate of the lattice strain of the {200} grains in the vertical sample decreases, indicating an additional load partitioning. At this point, the load is not taken up by other grain families, as all lattice plane families appear to shed load. It can be thus assumed that, at this stage, the load is partially transferred to the new forming phase(s). Indeed, at this point of the deformation, which corresponds to an applied strain of 1 %, hcp-ε peaks start to be detected in the vertical sample by neutron diffraction (Fig. 6-e). In the horizontal sample, the lattice strain of the {200} grains continues to increase linearly without any evidence of important load shedding at this deformation level.

3.4. In-situ EBSD

Fig. 8 shows the EBSD maps with phase coloring for a flat sample deformed up to 4 % strain. The same area is analyzed at different strain levels in order to characterize the formation of deformation-induced martensite.

At 1 % strain, hcp-ε is not detected within grain interior, although martensite formation is expected according to the decrease in the integrated intensity observed with neutron diffraction analysis (Fig. A6 in Appendix A). It is assumed that the lamellae thickness is below the detection limit of EBSD, considering the probe volume of the electrons of 50 nm³ for a single data point and the use of a step size of 80 nm. By increasing the macroscopic strain to 2 % and 4 %, hcp-ε lamellae are identified (Fig. 8-b). Some hcp-ε lamellae are still not fully indexed and appear as dark bands due to the limited thickness, indicating the characteristic inclination along the trace of one of the {1 1 1} planes.

In alloys with a low SFE, under an external load, a perfect dislocation on the {1 1 1} ⟨1 1 0⟩ slip system with high Schmid factor can
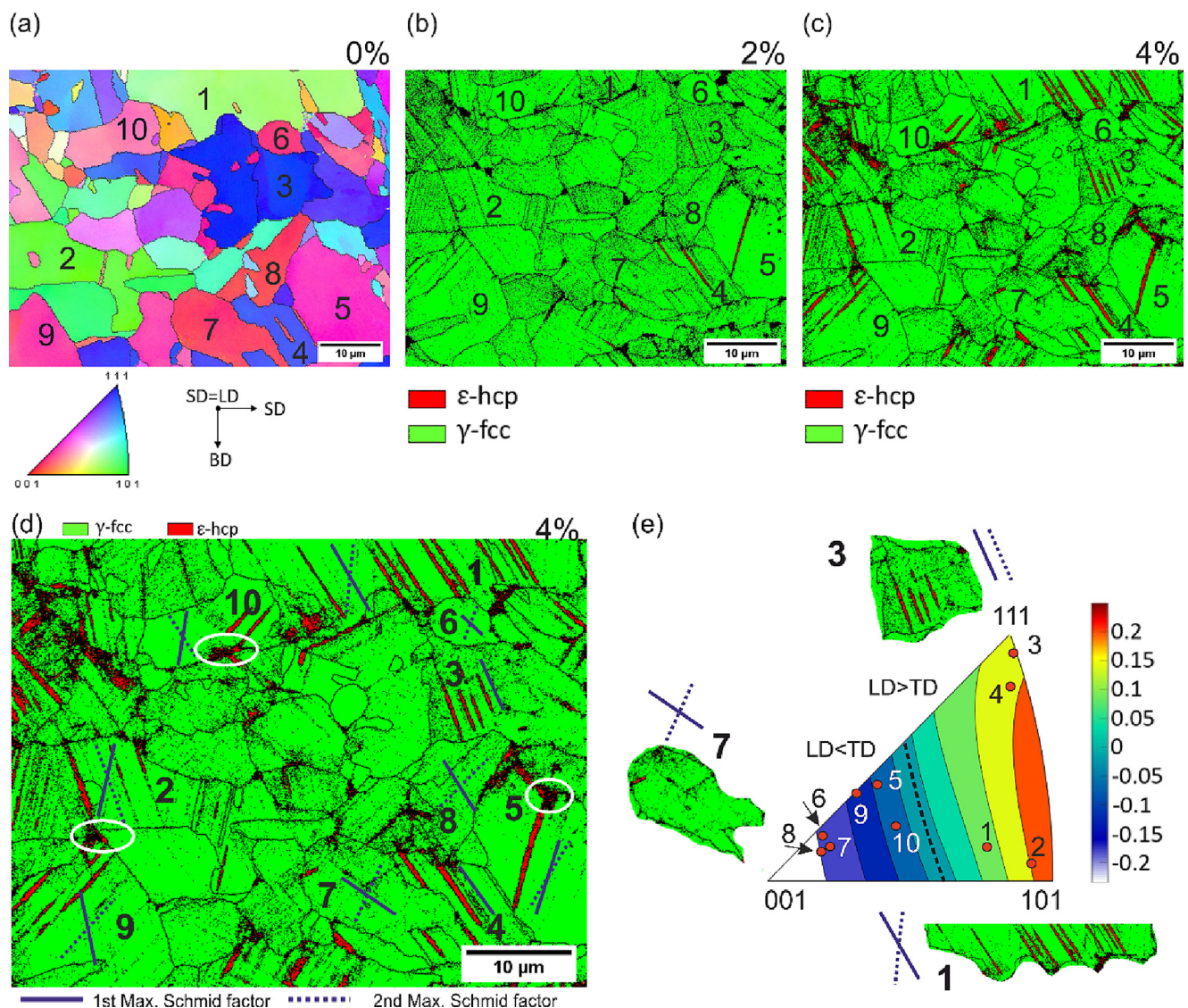

Fig. 8. EBSD map with IPF coloring related to the LD (a) and EBSD maps with phase coloring acquired during loading at 2 % (b) and 4 % strain (c) in a flat sample; EBSD map with phase coloring for horizontal flat sample at 4 % deformation obtained by in-situ EBSD showing the trace on the sample surface of the (1 1 1) ⟨1 1 0⟩ slip system with the maximum (blue line) and second maximum Schmid factor (blue dashed line) (d); IPF showing the difference in the Schmid factor of leading (LP) and trailing (TP) partial dislocations of type a/6 ⟨1 1 2⟩ dissociated from a perfect dislocation on the slip system {1 1 1} ⟨1 1 0⟩ (e); (For interpretation of the references to color in this figure legend, the reader is referred to the web version of this article.)

dissociate into a leading partial (LP) dislocation and a trailing partial (TP) dislocation of type a/6 ⟨112⟩. The Schmid factor of the individual LP and TP depends on the perfect dislocation from where they originated and on the orientation of the grain with respect to the LD. Table 2 and Fig. 8-e report the Schmid factor (LP and TP) of the SPDs, which form by dissociation of a perfect dislocation on the {111} ⟨110⟩ slip system with the highest Schmid factor. In Fig. 8-d, the slip trace with the maximum (solid blue line) and second maximum Schmid factor (blue dashed line) among the possible slip system {111} ⟨110⟩ are also plotted in the EBSD map with phase coloring (4 % strain) for few selected grains. It can be observed that for grains with orientation that lies on the right-hand side of the black dashed line boundary in the IPFs in Fig. 8-e, i.e. for grains with an orientation close to ⟨220⟩ or ⟨111⟩ along the LD, the Schmid factor of the LP is higher than that of the TP (LP > TP) if the dissociation of the perfect dislocation with the highest Schmid factor is considered.

Martensite lamellae form in different extent and size, depending on the grain orientation of the parent phase fcc-γ, as clearly visible from the three selected grains in Fig. 8-e, having orientation close to ⟨220⟩, ⟨200⟩ and ⟨111⟩. Grains with orientation close to ⟨220⟩ along the LD (grains 1–2) show the highest amount of hcp-ε phase. In these grains, LP > TP and martensite forms as thin lamellae homogenously distributed in the entire grain. In some cases, e.g. in grain 2, these lamellae appear as dark bands at 4 % due to the reduced thickness. Martensite profusely forms in lamellae aligned with the trace of the {111} ⟨110⟩ slip system with the highest Schmid factor. Martensite lamellae also form along the trace of the slip system with the second highest Schmid factor, which also shows LP > TP. In grains oriented close to the ⟨111⟩ direction in the LD (grains 3–4), hcp-ε lamellae are also observed in relatively high amount. For these grains, the Schmid factors of the leading partials are rather low (0.314 and 0.368) but still exceed the values of the respective trailing partials so that LP > TP.

Limited formation of martensite is observed for grains with an orientation close to ⟨311⟩ and ⟨200⟩ along the LD. These grains lay on the left-hand side of the black dashed line boundary in the IPFs in Fig. 8-e, meaning that if the perfect dislocation with the highest Schmid factor is considered, it applies LP < TP. No hcp-ε can be detected at 4 % strain in grains 6–7-8, for which the Schmid factor of TP significantly exceeds the Schmid factor of LP.

Only a reduced number of lamellae forms in grains 5–9-10. Despite LP < TP, few but thick martensite lamellae form, indicating that thickening of few lamellae rather than nucleation of multiple

lamellae seems to take place. As highlighted by the white marks in Fig. 8-d, hcp-ε lamellae seem to nucleate at the grain boundaries. Localized shear stresses at the grain boundaries can cause the growth of martensite at these locations [73].

3.5. In-situ DIC

In-situ DIC was performed to additionally investigate the amount and distribution of martensite within differently oriented grains. Fig. 9-a shows the EBSD map with IPF coloring for the sample prior to deformation.

Fig. 9-b,c, shows the DIC maps for the sample after deformation at 2 % (Fig. 9-b) and 4 % (Fig. 9-c) strain. The grain boundaries are designated with white lines on the maps. The DIC analysis reveals the localization of the strain, which gives an indication of strain accommodation by the formation of slip, SFs and martensitic transformation [74]. Already at 2 % strain, parallel bands with high ε_{eff} form within the grains. At 4 %, the values of ε_{eff} significantly increase. The orientation of the strain bands is similar to the microstructural dark bands and hcp-ε lamellae observed in the in-situ EBSD analysis, indicating the formation of martensite. As already observed by in-situ EBSD, the number and the width of bands vary between grains with different crystallographic orientations. Grains A and B, whose orientation is near to the ⟨220⟩ direction in the LD, show a rather homogenous strain distribution. Accommodated strains form thin but numerous bands within the grain interior. In grains with orientation between ⟨200-⟩ and ⟨311⟩ along the LD, which appear as red/violet in the EBSD map with IPF coloring, strains develop locally, with formation of less but wider bands characterized by high strain (grain E and F). For closely ⟨111⟩ -oriented grains (blue grains C, D), band distribution and size is between the {220} and {311}, {200} grains.

The ε_{eff} strains averaged within the grain at 4 % strain are reported for grain A and grains E and F, whose orientation and, therefore, Schmid factor for the LP and the TP are significantly different (Table 3). Grain A with an orientation close to the ⟨220⟩ direction along the LD and with LP > TP shows a higher number of strain bands homogeneously distributed within the grain (Fig. 9-d), which results in a total average strain of 3 % within the grain. The average strain associated with the martensitic transformation in grains F and E (LP-TP around −0.20) is significantly inferior to that of grain A, meaning that less strain is accommodated by transformation and/or slip compared to the previous case. Higher-strain bands but lower in number form indicating the formation of thick, localized, and more sporadic martensite lamellae (Fig. 9-d).

For the three individual grains, the {111} ⟨110⟩ systems with the highest and second highest Schmid factor are also reported (Fig. 9-d). In grain A, according to the orientation of the strain bands, most of the numerous martensite lamellae nucleate along the system with the highest Schmid factor. The system with the second highest Schmid factor is also activated, probably due to the fact that for this system LP > TP and the difference is particularly high (LP-TP = 0.354). Martensite lamellae along the two slip systems interact and intersect each other with high frequency and at different locations. In grain E lamellae also seem to preferentially form along the system with the highest or second highest Schmid factor, but to a limited extent. Despite for the first system LP < TP, for the second system LP-TP = 0.222. The martensite lamellae along the system with the highest Schmid factor tend to be rather thick and are not as numerous as in the grain A. In grain F, some martensite transformation also occurs along systems with lower Schmid factor, for which LP > TP. This indicates that the Schmid factor of LP and TP affects the amount and morphology of martensite that forms during loading and its nucleation is particularly pronounced along the systems for which LP > TP.

Table 2
Schmid factor of leading (LP) and trailing (TP) partial dislocations of type a/6 ⟨112⟩ dissociated from a perfect dislocation with the highest Schmid factor of the slip system {111} ⟨110⟩ for the differently oriented grains; the difference in the Schmid factor of the two partials is also reported (LP-TP); for the selected grains, grain orientation is defined by the plane normal to the LD;

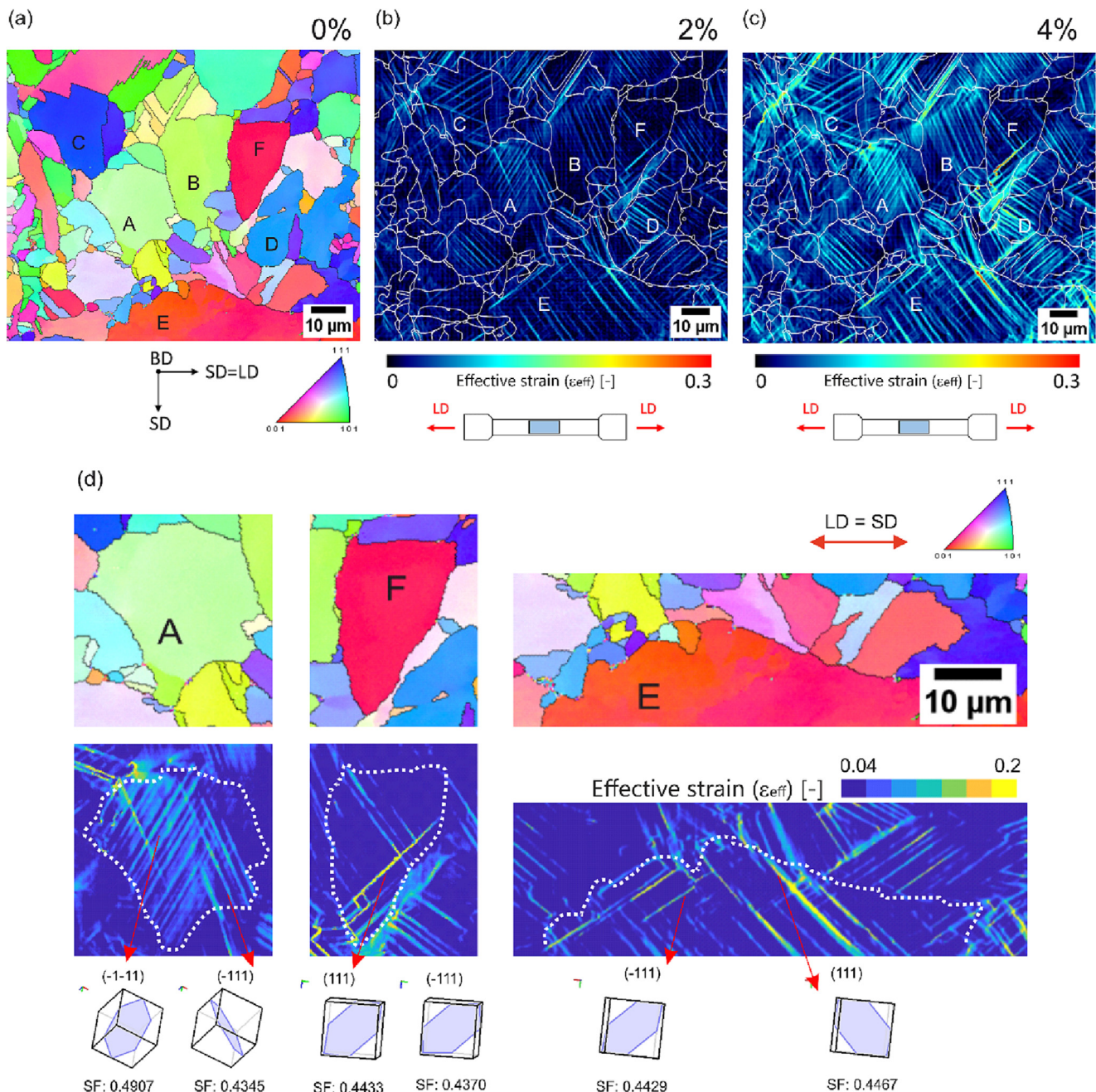| Grain	Grain orientation	LP	TP	LP-TP
1	(9 $\bar{1}$ 6)	0.415	0.119	0.063
2	(19 $\bar{15}$ 1)	0.477	0.318	0.159
3	(19 18 $\bar{20}$)	0.314	0.169	0.145
4	(12 12 $\bar{17}$)	0.368	0.236	0.132
5	(2 2 $\bar{7}$)	0.376	0.405	−0.029
6	(25 $\bar{4}$ 3)	0.330	0.462	−0.132
7	(23 4 2)	0.333	0.472	−0.139
8	(25 2 $\bar{3}$)	0.266	0.499	−0.233
9	(30 8 $\bar{7}$)	0.375	0.426	−0.051
10	($\bar{6}$ 25 $\bar{8}$)	0.314	0.346	−0.032

Fig. 9. EBSD map with IPF coloring related to the LD (a) and surface strain maps acquired during loading at 2 % (b) and 4 % strain (c) in a flat sample; a sketch of the investigated area is also reported; EBSD maps with IPF coloring and related surface strain maps for three selected grains (d); for the three selected grains, the {111} slip planes of the {111}⟨110⟩ systems with the highest and second highest Schmid factor are reported together with the calculated Schmid factor; the red arrows indicate the hcp-ε lamellae that nucleate along these planes; (For interpretation of the references to color in this figure legend, the reader is referred to the web version of this article.)

4. Discussion

4.1. Effect of grain orientation on martensite transformation(s)

According to the in-situ neutron diffraction analysis, the orientation of the LPBF-fabricated samples (vertical or horizontal in the build plate) affects the martensitic transformation induced during loading. Considering the peak intensity as a measure for the volume phase fraction in the samples, the increase of the hcp peak intensities with the applied deformation must be assigned to the transformation from fcc-γ austenite to hcp-ε martensite. The appearance of hcp-ε peaks at the lower applied strain (<2%) in the vertical sample compared to the absence in horizontal one

denotes an earlier and premature martensitic transformation for the former (Fig. 6-e,f). Additionally, the higher hcp-ε peak intensity values indicate that martensite forms to a larger extent when the sample is fabricated with a vertical orientation in the build plate, especially at low deformation levels.

The evolution of the micro-strain of the grain families of the vertical sample also gives evidence of pronounced martensitic transformation (Fig. 7). After yielding, the micro-strain within the {220} grains of the vertical sample does not change with increasing external stresses up to 400 MPa, indicating that grains start to behave plastically and additional stresses acting on these grains are relaxed by the fcc-γ → hcp-ε transformation [55]. The almost perfect plasticity of the {220} grains in the vertical sample results

Table 3

Grain orientation and Schmid factor of leading (LP) and trailing (TP) partial dislocations of type a/6 ⟨112⟩ dissociated from a perfect dislocation on the slip system {111} ⟨110⟩ with the highest Schmid factor; the average strain of the selected grains calculated by DIC is also reported; for the selected grains, grain orientation is defined by the plane normal to the LD;

Grain	Grain orientation	LP	TP	LP-TP	Average strain (%)
A	$(\overline{23}\,3\,15)$	0.476	0.368	0.108	3.0
F	$(\overline{13}\,1\,1)$	0.287	0.496	−0.209	1.0
E	$(\overline{33}\,1\,3)$	0.285	0.492	−0.207	1.8

in enhanced load transfer to the {200} grains, increasing the divergence between the two grain families. The {220} austenite grains of the horizontal sample also show a plastic behavior after yielding, which is mainly ascribed to the phase transformation to hcp-ε. However, the associated stress relaxation and load transfer to {200} grains is not as pronounced as in the vertical sample.

Above 275 MPa, the lattice strain accumulation slows down for the {111} grains and starts to decrease for the {220} grains of the vertical sample. At stress above 335 MPa, the {200} grains of the vertical sample also show a certain load shedding. At this point, part of the load is also shared with the transforming hcp-ε phase as the volume fraction of martensite induced by the deformation becomes sufficiently high to bear some load shed by the austenitic phase [68,69]. Similar behavior is not observed in the lattice strain of the austenite grains of the horizontal sample, possibly because of the reduced amount of martensite formation compared to the vertical sample at this point of the deformation.

With increasing strain, both hcp-ε and bcc-α′ form in the samples and the volume fraction of bcc-α′ martensite increases with deformation. According to neutron diffraction and magnetic induction investigations, the bcc-α′ formation occurs at a lower strain (peaks of bcc-α′ are already detected at 4 % strain-Fig. 6-f) and to a larger extent in the vertical sample compared to the horizontal one. The martensite transformations have been well studied in high-Mn steels showing the TRIP effect [75]. The main factors affecting martensitic transformations are SFE [76], chemical composition [16,77], temperature [32], and level of deformation [78,79]. Considering that bcc-α′ martensite is known to form from hcp-ε lamelle and their intersections [80,81], thus following the sequence fcc-γ → hcp-ε → bcc-α′ [50,82,83], the distinct amount of bcc-α′ martensite in the vertical and horizontal samples can be directly correlated to the distinct amount of the precursor phase hcp-ε.

The reason for the different transformation behavior observed for the two samples is ascribed to the preferential orientation of the grains along the LD. In previous neutron diffraction investigations on a similar alloy system but conventionally manufactured, a clear correlation between grain orientation with respect to the applied external load and martensite transformation has been found [56]. Under an external load, the dissociation of a/2 ⟨110⟩ perfect dislocations into SPDs of the type a/6 ⟨112⟩ is accomplished due to the low SFE of the system. The motion of a/6 ⟨112⟩ SPDs and the formation of SFs result in the nucleation of martensite, which proceeds by extension and overlap of the SFs on every second (111) plane of austenite [84,85]. During loading, the SF width changes based on the resolved shear stress on the LP and TP, thus on the Schmid factor of the LP and TP and the magnitude of the external load. A higher Schmid factor for the LP than for the TP usually results in an increase in the SF width and, therefore, in forming a high amount of nucleation sites for hcp-ε [86]. This explains the correlation between martensite formation and grain orientation/Schmid factor of SPDs observed in the in-situ EBSD and DIC analysis of the present study. A higher amount of martensite lamellae forms in the grains with orientations close to ⟨220⟩ in the LD, for which the Schmid factor of the LP is particularly high and LP > TP. The continuous nucleation and expansion of SFs expected for these grains result in pronounced martensite formation already at the very beginning of the deformation. Because of the high availability of SFs in these austenite grains, the nucleation of new martensite lamellae is favored, leading to the formation of dense and thin lamellae of martensite. According to high-resolution electron microscopy (TEM) investigations, the presence of uniformly scattered SFs in austenite promotes the formation of nanometric deformation bands that, in most of the cases, consist of a mixture of fcc-γ and hcp-ε phase. These thin hcp-ε martensite lamellae are readily reverse-transformed by recovery heating [87–89].

Nucleation and extension of SFs are not as favored in the grains ⟨200⟩- and ⟨311⟩ -closely oriented along the LD. The formation of martensite in these grains occurs at pre-existing SFs or is delayed until lower-Schmid factor slip systems for which LP > TP are activated under the application of external load. At the beginning of deformation, fewer nucleation sites for hcp-ε are generated. Strain is thus mainly accommodated by the thickening of a few localized hcp-ε lamellae rather than by the nucleation of new lamellae. This leads to the formation of thick martensite lamellae in confined areas of the grains, as observed by in-situ EBSD and DIC results. A higher deformation level is probably required for these grains to profusely transform within the grain interior.

In previous studies on conventionally fabricated SMAs [56], it was observed that martensite transformation is suppressed in those grains for which LP < TP because of the limited availability of nucleation sites for martensite. For the present alloy, although in an inferior amount, hcp-ε lamellae also form in the less-favorably oriented grains. This is mainly ascribed to the specific microstructure generated during the LPBF. After fabrication, the high concentration of grain boundaries and SFs provides effective nucleation sites for hcp-ε [56,73,90].

Neutron diffraction patterns prior deformation show that the orientation of the grains along the LD of the horizontal sample is rather random. In contrast, most grains in the vertical sample show a preferential ⟨220⟩ orientation, which favors the transformation of austenite, explaining the high volume fraction of hcp-ε and bcc-α′ induced in the vertical sample already at the first stages of the deformation.

4.2. Effect of sample orientation on the thermo-mechanical properties

The difference in the phase transformation behavior dictated by the distinct crystallographic texture of the horizontal and vertical samples affects the macroscopic mechanical behavior of the material. This is clearly visible from the comparison of the macroscopic stress–strain curves of the two samples. The gradual change from linearity in the investigated alloy is related to an elastic/plastic transition regime attributed to the formation of SFs and hcp-ε [55]. Thus, the premature onset of non-linearity in the stress–strain curve of the vertical sample compared to the horizontal one derives from the easier and earlier martensite transformation of the former. The lower yield point (both $\sigma_{0.1}$ and $\sigma_{0.2}$) indicates

that the stress to induce martensite has been decreased in the vertical sample [91].

Another important feature that can be accountable for the anisotropy of the LPBF-produced alloy is the different aspect ratio of the grains with respect to the LD [31]. As grains growth preferentially elongated parallel to the BD, the contribution of grain boundary strengthening is not isotropic. Considering that in the vertical sample the BD corresponds to the LD, it can be seen from Fig. 2 that the effective grain size along the LD is higher, and the number of grain boundaries is lower for the vertical sample compared to the horizontal one [92,93]. A lower grain boundary strengthening effect is thus expected for the vertical sample, resulting in inferior strength but higher elongation to failure. Furthermore, the more pronounced bcc-α' formation in the vertical sample than in the horizontal might also contribute to the higher elongation achieved for the former, as necking is delayed by the martensitic transformations fcc-γ → hcp-ε → bcc-α' [94].

A slight difference in the work hardening and plastic deformation behavior is also observed between the vertical and horizontal samples. The variation in the work hardening rate curves of the two samples is ascribed to the possible changes in the dominant deformation mechanisms and the balance between deformation mechanisms [71]. After the initial elastic strain, for true strain above 5 %, a less steep decreasing work hardening rate is observed for both samples, becoming particularly evident between 6 % and 8 % strain in the vertical sample. This variation in the work hardening rate is ascribed to the formation of hcp-ε lamellae that act as barriers to the dislocation motion within fcc-γ. The generation of geometrically necessary dislocations, which form at phase boundaries to ensure lattice compatibility, also contributes to locally strengthen the material [95]. Above 8 % strain, the work hardening rate of the vertical sample starts rising, probably due to a combination of an increasing amount of hcp-ε transformation and bcc-α' formation. The formation of bcc-α' martensite is particularly effective in increasing the strength of the material due to the higher strength of the phase [39] and due to the continuous microstructure refinement, which progressively reduces the free path (pinning) of dislocation (dynamic Hall-Petch effect) [7,66]. The work hardening of the horizontal sample reaches a relatively steady state and keeps decreasing at a constant rate. Because of the lower amount of hcp-ε and bcc-α' formation upon deformation, no increase in the work hardening is observed for the horizontal sample at this stage.

In most of the previous studies on conventionally fabricated Fe-Mn-Si-SMAs, many attempts have been made to improve the SME and PE. The SME could be significantly increased by the controlled precipitation of fine NbC [96], VC or VN [97], $Cr_{23}C_6$ [98]. The reason for the improvement is found in the generation of a high number of SFs accompanying the precipitation, which leads to the formation of very thin (<3 nm) martensite plates within austenite grains upon deformation [89]. A similar effect is obtained by the so-called "training". Samples are repeatedly deformed at RT, followed by an annealing process at 650–800 °C [99]. Training in Fe-based SMAs is employed to obtain a microstructure composed of fine austenite grains with evenly spaced and well-defined SFs throughout the parent phase. Samples processed via training produce a larger fraction of martensite compared to samples in the as-austenitized condition, as the generated SFs act as nucleation sites for martensite formation during deformation [91]. Additionally, the induced precipitation and grain refinement observed after training result in an improved SME and PE due to the increased amount of martensite hcp-ε lamellae interacting with grain boundaries and precipitates. Grain boundaries and precipitates are known to exert back stresses on the tip of hcp bands, promoting the reverse transformation to austenite [6,32,99,100]. However, costs and time for the production of the components increase sig-

nificantly when training is applied [101]. Sharpening the ⟨110⟩ texture component along the tensile axis of the fabricated components has also been suggested as a possible strategy to increase the SME [102]. Studies performed on hot-rolled Fe-Mn-Si show the formation of a larger ⟨110⟩ component in the rolling direction, which is beneficial for a good SME [32,103]. The development of such a texture is the result of thermomechanical treatments, which involve several steps of rolling at high temperatures (>1000 °C) [103]. However, the texture developed in hot-rolled components is rather weak as the majority of crystal grains are not strictly oriented to {001}⟨110⟩ but scatter more or less from the ideal {001}⟨110⟩. Additionally, this shear texture mainly develops at the surface and penetrates only to about a 30 % of the thickness of the components [102]. LPBF appears to be more suitable for the fabrication of samples with controlled crystallographic textures and, therefore, pronounced SME. In the present work, samples with a rather pronounced ⟨220⟩ texture could be manufactured simply by changing the build orientation. The higher amount of {220} grains obtained by fabricating the sample vertically (LD parallel to BD) rather than horizontally (LD perpendicular to BD) leads to an increase of almost 14 % in the recovery strain.

It is worth noting that enhanced SME is also achieved in the horizontal sample, with recovery strain values that are superior to those measured for the same alloy but conventionally manufactured and containing VC-precipitates (maximum ε_{rec} of 1.15 % [43,65]). This indicates that the integration of SMAs into AM allows for the fabrication of components with pronounced shape memory properties without the need for post thermo-mechanical processing. Significant grain refinement and formation of high density of SFs already occur during the LPBF process.

By increasing the pre-straining (10 %), the strain recovery after heating at 300 °C reduces in both the vertical and horizontal samples investigated in this study. The deterioration in the SME can be ascribed to the formation of bcc-α ′, as bcc-α' partially blocks or interferes with the reverse transformation of hcp-ε to fcc-γ responsible for the SME [89] and consumes the reversible hcp-ε phase by forming. As the vertical samples appear to contain a higher faction of bcc-α' than the horizontal ones, the strain recovery upon heating is inferior for the former when a higher level of pre-straining is applied. At higher deformation, in addition to the formation of bcc-α', which is irreversible, irrecoverable slip is also activated. The transition from deformation-induced martensite formation to irreversible slip is known to cause a significant decrease in SME [28,104]. In previous studies [71,105] on different alloy systems but also showing the TRIP effect (metastable high entropy alloys), it has been observed that at high strain levels, twinning in the hcp-ε phase also occurs along with fcc-γ → hcp-ε transformation. It has been reported that deformation twins lead to a marked decrease in the free slip length of dislocations, resulting in increased work hardening effect (Hall-Petch effect) [106]. Despite the effect of the twins on the reversibility of the martensite phase has not been discussed in these studies, a decrease in the SME with twin formation is expected. Due to the strong interaction with perfect and partial dislocations, deformation twins in hcp-ε can have the same effect of annealing twin boundaries, acting as obstacles for hcp-ε martensite formation and reversion and leading to annihilation or trapping of partials at the martensite tips [89]. Further investigations will be performed in the future in this regard.

The present results demonstrate the potential of AM for the fabrication of the investigated Fe-Mn-Si-based SMA. The dependence of the activated deformation mechanisms and, therefore, of the thermo-mechanical properties on the microstructure makes this material promising for the fabrication of parts with tunable functionalities. The texture formed in the LPBF-fabricated components, which is expected to be more pronounced compared to conven-

tionally processed SMAs [32], can be adjusted and controlled by varying the sample orientation according to the required performance. Strength of the components can be increased with the horizontal configuration and the related microstructure. Whereas, the preferential ⟨220⟩ grain orientation generated with the vertical orientation is beneficial to improve alloy's SME activated after low level of pre-straining.

5. Conclusions

In this study, the martensitic transformation fcc-γ → hcp-ε → bcc-α ′ are investigated by in-situ neutron diffraction and, complementary, by in-situ EBSD and DIC for a Fe-Mn-Si-based shape memory alloy fabricated by laser powder bed fusion. The effect of sample orientation on phase evolution is analyzed and correlated with the deformation behavior, the alloy's shape memory and mechanical properties. Two sets of samples are compared: the vertical sample, for which the loading direction (LD) is parallel to the build direction (BD), and the horizontal sample, where the LD is perpendicular to the BD. The following conclusions can be made:

1. Different crystallographic textures can be generated along the LD of the samples by varying the sample orientation with respect to the BD. As grains show a preferential ⟨110⟩ orientation along the BD, the vertical sample shows a ⟨110⟩ texture along the LD.
2. The {220} austenite grains easily transform to hcp-ε due to their high Schmid factor of the leading partial dislocation dissociated from the perfect dislocation with the highest Schmid factor. In those grains, hcp-ε martensite forms as thin lamellae homogenously distributed within the grain interior already at low deformation levels. Other grain families appear to transform as well, although in an inferior amount, due to the existence of SFs in the as-built condition and the very fine microstructure and low SFE of the alloy.
3. More pronounced fcc-γ → hcp-ε → bcc-α ′ transformation occurs in the vertical sample compared to the horizontal sample due to high population of {220} grains along the LD, which profusely transform during loading.
4. The different transformation behavior of the vertical and horizontal samples results in differences in the shape memory effect, as well as in the mechanical properties and the deformation behavior of the investigated material.

The current results show the great potential of laser powder bed fusion for the fabrication of Fe-based shape memory alloys, whose functional properties strongly depend on the texture and microstructure inherited by the processing parameters. By simply modifying the processing conditions, such as the build orientation, mechanical and shape memory properties can be tuned according to the specific applications.

CRediT authorship contribution statement

I. Ferretto: Conceptualization, Methodology, Validation, Investigation, Data curation, Visualization, Writing – original draft. **D. Kim:** Validation, Investigation. **W.J. Lee:** Conceptualization, Writing – review & editing, Supervision. **E. Hosseini:** Validation, Investigation, Writing – review & editing. **N.M. della Ventura:** Validation, Investigation. **A. Sharma:** Validation, Investigation, Writing – review & editing. **C. Sofras:** Investigation. **J. Capek:** Validation, Investigation. **E. Polatidis:** Validation, Investigation, Conceptualization, Writing – review & editing. **C. Leinenbach:** Conceptualization, Writing – review & editing, Project administration, Supervision.

Data availability

Data will be made available on request.

Declaration of Competing Interest

The authors declare that they have no known competing financial interests or personal relationships that could have appeared to influence the work reported in this paper.

Acknowledgement

Data availability

The data that support the findings of this study are available from the corresponding author upon reasonable request.

Appendix A. Supplementary material

Supplementary data to this article can be found online at https://doi.org/10.1016/j.matdes.2023.111928.

References

[1] L. Janke, C. Czaderski, M. Motavalli, J. Ruth, Applications of shape memory alloys in civil engineering structures—overview, limits and new ideas, Mat. Struct. 38 (2005) 578–592, https://doi.org/10.1007/BF02479550.
[2] M. Balasubramanian, R. Srimath, L. Vignesh, S. Rajesh, Application of shape memory alloys in engineering – a review, J. Phys.: Conf. Ser. 2054 (2021), https://doi.org/10.1088/1742-6596/2054/1/012078 012078.
[3] A. Cladera, B. Weber, C. Leinenbach, C. Czaderski, M. Shahverdi, M. Motavalli, Iron-based shape memory alloys for civil engineering structures: an overview, Constr. Build. Mater. 63 (2014) 281–293, https://doi.org/10.1016/j.conbuildmat.2014.04.032.
[4] A. Sato, E. Chishima, K. Soma, T. Mori, Shape memory effect in γ⇄ε transformation in Fe-30Mn-1Si alloy single crystals, Acta Metall. (1982), https://doi.org/10.1016/0001-6160(82)90011-6.
[5] S. Jiang, Y. Wang, B. Yan, Y. Zhang, Hot workability of FeMnSiCrNi shape memory alloy based on processing map and martensitic transformation, J. Alloy. Compd. 806 (2019) 1153–1165, https://doi.org/10.1016/j.jallcom.2019.07.316.
[6] N. Bergeon, G. Guenin, C. Esnouf, Microstructural analysis of the stress-induced ε martensite in a Fe–Mn–Si–Cr–Ni shape memory alloy: Part II: Transformation reversibility, Mater. Sci. Eng. A 242 (1998) 87–95, https://doi.org/10.1016/S0921-5093(97)00512-1.
[7] A. Druker, A. Perotti, I. Esquivel, J. Malarría, A manufacturing process for shaft and pipe couplings of Fe-Mn-Si-Ni-Cr shape memory alloys, Mater. Des. 56 (2014) 878–888, https://doi.org/10.1016/j.matdes.2013.11.032.
[8] S. Jiang, Y. Wang, Y. Zhang, X. Xing, Role of stacking faults in martensite transformation of FeMnSiCrNi shape memory alloy subjected to plastic deformation at high temperatures, Intermetallics 124 (2020), https://doi.org/10.1016/j.intermet.2020.106841 106841.
[9] S. Jiang, Y. Wang, X. Xing, Y. Zhang, Stress-induced martensite phase transformation of FeMnSiCrNi shape memory alloy subjected to mechanical vibrating polishing, Trans. Nonferrous Met. Soc. Chin. 30 (2020) 1582–1593, https://doi.org/10.1016/S1003-6326(20)65321-3.
[10] B. Jiang, X. Qi, S. Yang, W. Zhou, T.Y. Hsu (Xu Zuyao), Effect of stacking fault probability on γ–ε martensitic transformation and shape memory effect in Fe–Mn–Si based alloys, Acta Materialia. 46 (1998) 501–510, doi: 10.1016/S1359-6454(97)00266-8.
[11] Z. Guo, Y. Rong, S. Chen, T.Y.H. (Xu Zuyao), Energy consideration of the fcc (γ)→hcp(ε) martensitic transformation in Fe–Mn–Si based Alloys, Materials Transactions, JIM 40 (1999) 328–334, doi: 10.2320/matertrans1989.40.328.
[12] J. Xuejun, Z. Jihua, T.Y. Hsu, Thermodynamic calculation of stacking fault energy in Fe–Mn–Si shape memory alloys, Mater. Des. 21 (2000) 537–539, https://doi.org/10.1016/S0261-3069(00)00006-6.
[13] D.T. Pierce, J. JimÉNEZ, J. Bentley, D. Raabe, J.E. Wittig, The influence of stacking fault energy on the microstructural and strain-hardening evolution

of Fe-Mn-Al-Si steels during tensile deformation, Acta Mater. 100 (2015) 178–190, https://doi.org/10.1016/j.actamat.2015.08.030.

[14] J. Talonen, H. Hänninen, Formation of shear bands and strain-induced martensite during plastic deformation of metastable austenitic stainless steels, Acta Mater. 55 (2007) 6108–6118, https://doi.org/10.1016/j.actamat.2007.07.015.

[15] C. Ullrich, S. Martin, C. Schimpf, A. Stark, N. Schell, D. Rafaja, Deformation mechanisms in metastable austenitic TRIP/TWIP steels under compressive load studied by in situ synchrotron radiation diffraction, Adv. Eng. Mater. 21 (2019) 1801101, https://doi.org/10.1002/adem.201801101.

[16] A. Collazo, R. Figueroa, C. Mariño-Martínez, C. Pérez, Microstructure and thermomechanical characterization of Fe-28Mn-6Si-5Cr shape memory alloy, Metals 11 (2021) 649, https://doi.org/10.3390/met11040649.

[17] D. Wang, W. Ji, M. Han, D. Jia, W. Liu, Influence of ausforming on substructures and shape memory behavior in Fe-28Mn-6Si-5Cr alloy, Mater. Sci. Forum 327 (2000) 263–266, https://doi.org/10.4028/www.scientific.net/msf.327-328.263.

[18] Q. Zou, X. Ye, Y. Li, W. Luo, X. Yang, Y. Luo, Effects of Ti on microstructure and properties of Fe–Mn–Si–Cr–Ni shape memory alloy, Mater. Chem. Phys. 293 (2023), https://doi.org/10.1016/j.matchemphys.2022.126992 126992.

[19] Y. Yang, C. Leinenbach, M. Shahverdi, Simulation and experimental characterization of VC precipitation and recovery stress formation in an FeMnSi-based shape memory alloy, J. Alloy. Compd. 940 (2023), https://doi.org/10.1016/j.jallcom.2023.168856 168856.

[20] H. Khodaverdi, M. Mohri, A.S. Ghorabaei, E. Ghafoori, M. Nili-Ahmadabadi, Effect of low-temperature precipitates on microstructure and pseudoelasticity of an Fe–Mn–Si-based shape memory alloy, Mater Charact 195 (2023), https://doi.org/10.1016/j.matchar.2022.112486 112486.

[21] H.B. Peng, J.B. Zhang, L.X. Sun, F. Song, X.G. An, H. Wang, Y.H. Wen, Evolution of shape memory effect with aging time during aging after pre-strain in Fe–Mn–Si–Cr–Ni–C shape memory alloys, Mater. Sci. Eng. A 852 (2022), https://doi.org/10.1016/j.msea.2022.143675.

[22] R.T. van Tol, J.K. Kim, L. Zhao, J. Sietsma, B.C. De Cooman, α′-Martensite formation in deep-drawn Mn-based TWIP steel, J. Mater. Sci. 47 (2012) 4845–4850, https://doi.org/10.1007/s10853-012-6345-y.

[23] Q. Lai, P. Song, H. Zhou, L. Xiao, T. Feng, C. Li, Deformation-induced martensitic transformation and strain hardening in a nanocrystalline FeMn alloy processed by severe austenite pre-deformation, Materialia. 13 (2020), https://doi.org/10.1016/j.mtla.2020.100832 100832.

[24] M.J. Sohrabi, M. Naghizadeh, H. Mirzadeh, Deformation-induced martensite in austenitic stainless steels: a review, Archiv. Civ. Mech. Eng. 20 (2020) 124, https://doi.org/10.1007/s43452-020-00130-1.

[25] C. Liu, Q. Peng, Z. Xue, S. Wang, C. Yang, Microstructure and mechanical properties of hot- rolled and cold-rolled medium-Mn TRIP steels, Materials 11 (2018) 2242, https://doi.org/10.3390/ma11112242.

[26] L. Bracke, J. Penning, N. Akdut, The influence of Cr and N additions on the mechanical properties of FeMnC steels, Metall Mater Trans A. 38 (2007) 520–528, https://doi.org/10.1007/s11661-006-9084-3.

[27] H.E. Sabzi, A. Zarei-Hanzaki, H.R. Abedi, A. Mateo, J.J. Roa, The sequential twinning-transformation induced plasticity effects in a thermomechanically processed high Mn austenitic steel, Mater. Sci. Eng. A 725 (2018) 242–249, https://doi.org/10.1016/j.msea.2018.03.102.

[28] W.J. Lee, B. Weber, G. Feltrin, C. Czaderski, M. Motavalli, C. Leinenbach, Phase transformation behavior under uniaxial deformation of an Fe–Mn–Si–Cr–Ni–VC shape memory alloy, Mater. Sci. Eng. A 581 (2013) 1–7, https://doi.org/10.1016/j.msea.2013.06.002.

[29] T. DebRoy, H.L. Wei, J.S. Zuback, T. Mukherjee, J.W. Elmer, J.O. Milewski, A.M. Beese, A. Wilson-Heid, A. De, W. Zhang, Additive manufacturing of metallic components – process, structure and properties, Prog. Mater Sci. 92 (2018) 112–224, https://doi.org/10.1016/j.pmatsci.2017.10.001.

[30] J. Günther, F. Brenne, M. Droste, M. Wendler, O. Volkova, H. Biermann, T. Niendorf, Design of novel materials for additive manufacturing - Isotropic microstructure and high defect tolerance, Sci Rep. 8 (2018) 1298, https://doi.org/10.1038/s41598-018-19376-0.

[31] C. Haase, J. Bültmann, J. Hof, S. Ziegler, S. Bremen, C. Hinke, A. Schwedt, U. Prahl, W. Bleck, Exploiting process-related advantages of selective laser melting for the production of high-manganese steel, Materials (Basel) 10 (2017), https://doi.org/10.3390/ma10010056.

[32] A. Arabi-Hashemi, W.J. Lee, C. Leinenbach, Recovery stress formation in FeMnSi based shape memory alloys: Impact of precipitates, texture and grain size, Mater. Des. 139 (2018) 258–268, https://doi.org/10.1016/j.matdes.2017.11.006.

[33] M. Soleimani, A. Kalhor, H. Mirzadeh, Transformation-induced plasticity (TRIP) in advanced steels: a review, Mater. Sci. Eng. A 795 (2020), https://doi.org/10.1016/j.msea.2020.140023 140023.

[34] M. Ma, Z. Wang, X. Zeng, A comparison on metallurgical behaviors of 316L stainless steel by selective laser melting and laser cladding deposition, Mater. Sci. Eng.: A C (2017) 265–273, https://doi.org/10.1016/j.msea.2016.12.112.

[35] Y.J. Yin, J.Q. Sun, J. Guo, X.F. Kan, D.C. Yang, Mechanism of high yield strength and yield ratio of 316 L stainless steel by additive manufacturing, Mater. Sci. Eng. A 744 (2019) 773–777, https://doi.org/10.1016/j.msea.2018.12.092.

[36] Y. Brif, M. Thomas, I. Todd, The use of high-entropy alloys in additive manufacturing, Scr. Mater. 99 (2015) 93–96, https://doi.org/10.1016/j.scriptamat.2014.11.037.

[37] L. Liu, Q. Ding, Y. Zhong, J. Zou, J. Wu, Y.-L. Chiu, J. Li, Z. Zhang, Q. Yu, Z. Shen, Dislocation network in additive manufactured steel breaks strength–ductility

trade-off, Mater. Today 21 (2018) 354–361, https://doi.org/10.1016/j.mattod.2017.11.004.

[38] Q.B. Nguyen, Z. Zhu, F.L. Ng, B.W. Chua, S.M.L. Nai, J. Wei, High mechanical strengths and ductility of stainless steel 304L fabricated using selective laser melting, J. Mater. Sci. Technol. 35 (2019) 388–394, https://doi.org/10.1016/j.jmst.2018.10.013.

[39] E. Polatidis, J. Čapek, A. Arabi-Hashemi, C. Leinenbach, M. Strobl, High ductility and transformation-induced-plasticity in metastable stainless steel processed by selective laser melting with low power, Scr. Mater. 176 (2020) 53–57, https://doi.org/10.1016/j.scriptamat.2019.09.035.

[40] T. Niendorf, F. Brenne, Steel showing twinning-induced plasticity processed by selective laser melting — an additively manufactured high performance material, Mater Charact 85 (2013) 57–63, https://doi.org/10.1016/j.matchar.2013.08.010.

[41] Y.M. Wang, T. Voisin, J.T. McKeown, J. Ye, N.P. Calta, Z. Li, Z. Zeng, Y. Zhang, W. Chen, T.T. Roehling, R.T. Ott, M.K. Santala, P.J. Depond, M.J. Matthews, A.V. Hamza, T. Zhu, Additively manufactured hierarchical stainless steels with high strength and ductility, Nat. Mater. 17 (2018) 63–71, https://doi.org/10.1038/nmat5021.

[42] I. Ferretto, D. Kim, N.M. Della Ventura, M. Shahverdi, W. Lee, C. Leinenbach, Laser powder bed fusion of a Fe–Mn–Si shape memory alloy, Addit. Manuf. 46 (2021) https://doi.org/10.1016/j.addma.2021.102071 102071.

[43] M. Koster, W.J. Lee, M. Schwarzenberger, C. Leinenbach, Cyclic deformation and structural fatigue behavior of an FE–Mn–Si shape memory alloy, Mater. Sci. Eng. A 637 (2015) 29–39, https://doi.org/10.1016/j.msea.2015.04.028.

[44] D. Kim, I. Ferretto, W. Kim, C. Leinenbach, W. Lee, Effect of post-heat treatment conditions on shape memory property in 4D printed Fe–17Mn–5Si–10Cr–4Ni shape memory alloy, Mater. Sci. Eng. A 852 (2022), https://doi.org/10.1016/j.msea.2022.143689 143689.

[45] I. Ferretto, D. Kim, M. Mohri, E. Ghafoori, W.J. Lee, C. Leinenbach, Shape recovery performance of a (V, C)-containing Fe–Mn–Si–Ni–Cr shape memory alloy fabricated by laser powder bed fusion, J. Mater. Res. Technol. 20 (2022) 3969–3984, https://doi.org/10.1016/j.jmrt.2022.08.143.

[46] R. Shi, S.A. Khairallah, T.T. Roehling, T.W. Heo, J.T. McKeown, M.J. Matthews, Microstructural control in metal laser powder bed fusion additive manufacturing using laser beam shaping strategy, Acta Mater. 184 (2020) 284–305, https://doi.org/10.1016/j.actamat.2019.11.053.

[47] M. Amirjan, H. Sakiani, Effect of scanning strategy and speed on the microstructure and mechanical properties of selective laser melted IN718 nickel-based superalloy, Int. J. Adv. Manuf. Technol. 103 (2019) 1769–1780, https://doi.org/10.1007/s00170-019-03545-0.

[48] S. Griffiths, M.D. Rossell, J. Croteau, N.Q. Vo, D.C. Dunand, C. Leinenbach, Effect of laser rescanning on the grain microstructure of a selective laser melted Al-Mg-Zr alloy, Mater Charact 143 (2018) 34–42, https://doi.org/10.1016/j.matchar.2018.03.033.

[49] A. Leicht, C.H. Yu, V. Luzin, U. Klement, E. Hryha, Effect of scan rotation on the microstructure development and mechanical properties of 316L parts produced by laser powder bed fusion, Mater Charact 163 (2020), https://doi.org/10.1016/j.matchar.2020.110309 110309.

[50] C. Sofras, J. Čapek, A. Arabi-Hashemi, C. Leinenbach, M. Frost, K. An, R.E. Logé, M. Strobl, E. Polatidis, Tailored deformation behavior of 304L stainless steel through control of the crystallographic texture with laser-powder bed fusion, Mater. Des. 219 (2022), https://doi.org/10.1016/j.matdes.2022.110789 110789.

[51] A. Leicht, U. Klement, E. Hryha, Effect of build geometry on the microstructural development of 316L parts produced by additive manufacturing, Mater Charact 143 (2018) 137–143, https://doi.org/10.1016/j.matchar.2018.04.040.

[52] T. Niendorf, F. Brenne, P. Krooß, M. Vollmer, D. Günther, D. Schwarze, H. Biermann, Microstructural evolution and functional properties of Fe-Mn-Al-Ni shape memory alloy processed by selective laser melting, Metall Mater Trans A. 47 (2016) 2569–2573, https://doi.org/10.1007/s11661-016-3412-z.

[53] I. Ferretto, A. Borzì, D. Kim, N.M.D. Ventura, E. Hosseini, W.J. Lee, C. Leinenbach, Control of microstructure and shape memory properties of a Fe-Mn-Si-based shape memory alloy during laser powder bed fusion, Additive Manuf. Lett. 3 (2022), https://doi.org/10.1016/j.addlet.2022.100091 100091.

[54] D. Kim, I. Ferretto, J.B. Jeon, C. Leinenbach, W. Lee, Formation of metastable bcc-δ phase and its transformation to fcc-γ in laser powder bed fusion of Fe–Mn–Si shape memory alloy, J. Mater. Res. Technol. 14 (2021) 2782–2788, https://doi.org/10.1016/j.jmrt.2021.08.119.

[55] C. Leinenbach, A. Arabi-Hashemi, W.J. Lee, A. Lis, M. Sadegh-Ahmadi, S. Van Petegem, T. Panzner, H. Van Swygenhoven, Characterization of the deformation and phase transformation behavior of VC-free and VC-containing FeMnSi-based shape memory alloys by in situ neutron diffraction, Mater. Sci. Eng. A 703 (2017) 314–323, https://doi.org/10.1016/j.msea.2017.07.077.

[56] A. Arabi-Hashemi, E. Polatidis, M. Smid, T. Panzner, C. Leinenbach, Grain orientation dependence of the forward and reverse fcc ↔ hcp transformation in FeMnSi-based shape memory alloys studied by in situ neutron diffraction, Mater. Sci. Eng. A 782 (2020), https://doi.org/10.1016/j.msea.2020.139261 139261.

[57] E.C. Oliver, T. Mori, M.R. Daymond, P.J. Withers, Comparison using neutron diffraction of martensitic transformation in Fe–Mn–Si shape memory alloys with and without VN precipitates, Mater. Sci. Technol. 24 (2008) 902–907, https://doi.org/10.1179/174328408X302576.

[58] D. Kim, I. Ferretto, C. Leinenbach, W. Lee, 3D and 4D printing of complex structures of Fe·Mn·Si-based shape memory alloy using laser powder bed fusion, Adv. Mater. Interfaces n/a (n.d.) 2200171, doi: 10.1002/admi.202200171.

[59] F. Di Gioacchino, J. Quinta da Fonseca, Plastic strain mapping with sub-micron resolution using digital image correlation, Exp Mech. 53 (2013) 743–754, https://doi.org/10.1007/s11340-012-9685-2.

[60] M. Hauser, M. Wendler, A. Weiß, J. Mola, Quantification of deformation-induced α′-martensite content in Fe-19Cr-3Mn-4Ni-0.15C-0.17N austenitic stainless steel by in-situ magnetic measurements, in: 2015.

[61] O. Arnold, J.C. Bilheux, J.M. Borreguero, A. Buts, S.I. Campbell, L. Chapon, M. Doucet, N. Draper, R. Ferraz Leal, M.A. Gigg, V.E. Lynch, A. Markvardsen, D.J. Mikkelson, R.L. Mikkelson, R. Miller, K. Palmen, P. Parker, G. Passos, T.G. Perring, P.F. Peterson, S. Ren, M.A. Reuter, A.T. Savici, J.W. Taylor, R.J. Taylor, R. Tolchenov, W. Zhou, J. Zikovsky, Mantid—Data analysis and visualization package for neutron scattering and μ SR experiments, Nucl. Instrum. Methods Phys. Res., Sect. A 764 (2014) 156–166, https://doi.org/10.1016/j.nima.2014.07.029.

[62] J. Blaber, B. Adair, A. Antoniou, Ncorr: open-source 2D digital image correlation matlab software, Exp Mech. 55 (2015) 1105–1122, https://doi.org/10.1007/s11340-015-0009-1.

[63] M.D. Atkinson, J.M. Donoghue, J.Q. da Fonseca, Measurement of local plastic strain during uniaxial reversed loading of nickel alloy 625, Mater Charact 168 (2020), https://doi.org/10.1016/j.matchar.2020.110561 110561.

[64] Y. Yang, A. Arabi-Hashemi, C. Leinenbach, M. Shahverdi, Influence of thermal treatment conditions on recovery stress formation in an FeMnSi-SMA, Mater. Sci. Eng. A 802 (2021), https://doi.org/10.1016/j.msea.2020.140694 140694.

[65] W.J. Lee, B. Weber, G. Feltrin, C. Czaderski, M. Motavalli, C. Leinenbach, Phase transformation behavior under uniaxial deformation of an Fe-Mn-Si-Cr-Ni-VC shape memory alloy, Mater. Sci. Eng. A 581 (2013) 1–7, https://doi.org/10.1016/j.msea.2013.06.002.

[66] T. Voisin, J.-B. Forien, A. Perron, S. Aubry, N. Bertin, A. Samanta, A. Baker, Y.M. Wang, New insights on cellular structures strengthening mechanisms and thermal stability of an austenitic stainless steel fabricated by laser powder-bed-fusion, Acta Mater. 203 (2021), https://doi.org/10.1016/j.actamat.2020.11.018 116476.

[67] Y. Onuki, S. Sato, In situ observation for deformation-induced martensite transformation during tensile deformation of SUS 304 stainless steel by using neutron diffraction PART II: Transformation and texture formation mechanisms, Quantum Beam Sci. 5 (2021) 6, https://doi.org/10.3390/qubs5010006.

[68] M. Humbert, B. Petit, B. Bolle, N. Gey, Analysis of the γ-ε-α′ variant selection induced by 10% plastic deformation in 304 stainless steel at −60°C, Mater. Sci. Eng. A 454–455 (2007) 508–517, https://doi.org/10.1016/j.msea.2006.11.112.

[69] M. Naeem, H. He, F. Zhang, H. Huang, S. Harjo, T. Kawasaki, B. Wang, S. Lan, Z. Wu, F. Wang, Y. Wu, Z. Lu, Z. Zhang, C.T. Liu, X.-L. Wang, Cooperative deformation in high-entropy alloys at ultralow temperatures, Sci. Adv. (2020), https://doi.org/10.1126/sciadv.aax4002.

[70] M.R. Daymond, M.a.M. Bourke, R.B. Von Dreele, B. Clausen, T. Lorentzen, Use of Rietveld refinement for elastic macrostrain determination and for evaluation of plastic strain history from diffraction spectra, J. Appl. Phys. 82 (1997) 1554–1562, doi: 10.1063/1.365956.

[71] E. Polatidis, S. Shukla, J. Čapek, S. Van Petegem, N. Casati, R.S. Mishra, Unveiling the interplay of deformation mechanisms in a metastable high entropy alloy with tuned composition using synchrotron X-ray diffraction, Mater. Today Commun. 30 (2022) 103155, https://doi.org/10.1016/j.mtcomm.2022.103155.

[72] S.F. Liu, Y. Wu, H.T. Wang, W.T. Lin, Y.Y. Shang, J.B. Liu, K. An, X.J. Liu, H. Wang, Z.P. Lu, Transformation-reinforced high-entropy alloys with superior mechanical properties via tailoring stacking fault energy, J. Alloy. Compd. 792 (2019) 444–455, https://doi.org/10.1016/j.jallcom.2019.04.035.

[73] A. Arabi-Hashemi, Y. Guo, J. Michler, D. Casari, C. Leinenbach, X. Maeder, Stress induced martensite variants revealed by in situ high resolution electron backscatter diffraction (HR-EBSD), Mater. Des. 151 (2018) 83–88, https://doi.org/10.1016/j.matdes.2018.04.006.

[74] W.-N. Hsu, E. Polatidis, M. Šmíd, N. Casati, S. Van Petegem, H. Van Swygenhoven, Load path change on superelastic NiTi alloys: In situ synchrotron XRD and SEM DIC, Acta Mater. 144 (2018) 874–883, https://doi.org/10.1016/j.actamat.2017.11.035.

[75] S.T. Pisarik, D.C. Van Aken, Crystallographic orientation of the ε → α′ martensitic (athermal) transformation in a FeMnAlSi steel, Metall Mater Trans A. 45 (2014) 3173–3178, https://doi.org/10.1007/s11661-014-2303-4.

[76] G.B. Olson, M. Cohen, A general mechanism of martensitic nucleation: Part I. General concepts and the FCC → HCP transformation, Metall. Trans. A 7 (1976) 1897–1904, https://doi.org/10.1007/BF02659822.

[77] U. Sarı, T. Kırındı, Effect of Mn content on the austenite–martensite phases and magnetic properties in Fe–Mn–Co alloys, Mater. Chem. Phys. 130 (2011) 738–742, https://doi.org/10.1016/j.matchemphys.2011.07.063.

[78] N. Li, Y.D. Wang, W.J. Liu, Z.N. An, J.P. Liu, R. Su, J. Li, P.K. Liaw, In situ X-ray microdiffraction study of deformation-induced phase transformation in 304 austenitic stainless steel, Acta Mater. 64 (2014) 12–23, https://doi.org/10.1016/j.actamat.2013.11.001.

[79] N. Gey, B. Petit, M. Humbert, Electron backscattered diffraction study of ε/α′ martensitic variants induced by plastic deformation in 304 stainless steel, Metall. Mater. Trans. A: Phys. Metall. Mater. Sci. 36 (2005) 3291–3299, https://doi.org/10.1007/s11661-005-0003-9.

[80] S. Pramanik, A.A. Gazder, A.A. Saleh, E.V. Pereloma, Nucleation, coarsening and deformation accommodation mechanisms of ε-martensite in a high manganese steel, Mater. Sci. Eng. A 731 (2018) 506–519, https://doi.org/10.1016/j.msea.2018.06.024.

[81] L. Bracke, L. Kestens, J. Penning, Transformation mechanism of α′-martensite in an austenitic Fe–Mn–C–N alloy, Scr. Mater. 57 (2007) 385–388, https://doi.org/10.1016/j.scriptamat.2007.05.003.

[82] E. Polatidis, W.-N. Hsu, M. Šmíd, T. Panzner, S. Chakrabarty, P. Pant, H. Van Swygenhoven, Suppressed martensitic transformation under biaxial loading in low stacking fault energy metastable austenitic steels, Scr. Mater. 147 (2018) 27–32, https://doi.org/10.1016/j.scriptamat.2017.12.026.

[83] C. Ullrich, S. Martin, C. Schimpf, H.-G. Brokmeier, N. Schell, A. Stark, D. Rafaja, Competition of mechanisms contributing to the texture formation in metastable austenitic steel under compressive load, Mater Charact 176 (2021), https://doi.org/10.1016/j.matchar.2021.111132 111132.

[84] Y. Ma, W. Song, W. Bleck, Investigation of the microstructure evolution in a Fe-17Mn-1.5Al-0.3C steel via in situ synchrotron X-ray diffraction during a tensile test, Materials 10 (2017) 1129, https://doi.org/10.3390/ma10101129.

[85] H. Li, D. Dunne, N. Kennon, Factors influencing shape memory effect and phase transformation behaviour of Fe–Mn–Si based shape memory alloys, Mater. Sci. Eng. A 273–275 (1999) 517–523, https://doi.org/10.1016/S0921-5093(99)00391-3.

[86] T.S. Byun, On the stress dependence of partial dislocation separation and deformation microstructure in austenitic stainless steels, Acta Mater. 51 (2003) 3063–3071, https://doi.org/10.1016/S1359-6454(03)00117-4.

[87] E.P. Kwon, S. Fujieda, K. Shinoda, S. Suzuki, Texture evolution and fcc/hcp transformation in Fe–Mn–Si–Cr alloys by tensile deformation, Mater. Sci. Eng. A 527 (2010) 6524–6532, https://doi.org/10.1016/j.msea.2010.06.041.

[88] S. Kajiwara, Characteristic features of shape memory effect and related transformation behavior in Fe-based alloys, Mater. Sci. Eng. A 273–275 (1999) 67–88, https://doi.org/10.1016/S0921-5093(99)00290-7.

[89] M.J. Lai, Y.J. Li, L. Lillpopp, D. Ponge, S. Will, D. Raabe, On the origin of the improvement of shape memory effect by precipitating VC in Fe–Mn–Si-based shape memory alloys, Acta Materialia 155 (n.d.) 222–235.

[90] A. Bauer, A. Vollmer, T. Niendorf, Effect of crystallographic orientation and grain boundaries on martensitic transformation and superelastic response of oligocrystalline Fe–Mn–Al–Ni shape memory alloys, Shap. Mem. Superelasticity. 7 (2021) 373–382, https://doi.org/10.1007/s40830-021-00340-3.

[91] N. Stanford, D.P. Dunne, Thermo-mechanical processing and the shape memory effect in an Fe–Mn–Si-based shape memory alloy, Mater. Sci. Eng. A 422 (2006) 352–359, https://doi.org/10.1016/j.msea.2006.02.009.

[92] M. El-Tahawy, P. Jenei, T. Kolonits, G. Han, H. Park, H. Choe, J. Gubicza, Different evolutions of the microstructure, texture, and mechanical performance during tension and compression of 316L stainless steel, Metall Mater Trans A. 51 (2020) 3447–3460, https://doi.org/10.1007/s11661-020-05782-5.

[93] Q. Xie, Z. Pei, J. Liang, D. Yu, Z. Zhao, P. Yang, R. Li, M. Eisenbach, K. An, Transition from the twinning induced plasticity to the γ-ε transformation induced plasticity in a high manganese steel, Acta Mater. 161 (2018) 273–284, https://doi.org/10.1016/j.actamat.2018.09.020.

[94] S. Martin, S. Wolf, U. Martin, L. Krüger, A. Jahn, Investigations on martensite formation in CrMnNi-TRIP steels, in: ESOMAT 2009 - 8th European Symposium on Martensitic Transformations, EDP Sciences, Prague, Czech Republic, 2009, p. 05022. doi: 10.1051/esomat/200905022.

[95] J.F. Nye, Some geometrical relations in dislocated crystals, Acta Metall. 1 (1953) 153–162, https://doi.org/10.1016/0001-6160(53)90054-6.

[96] Z.Z. Dong, S. Kajiwara, T. Kikuchi, T. Sawaguchi, Effect of pre-deformation at room temperature on shape memory properties of stainless type Fe–15Mn–5Si–9Cr–5Ni–(0.5–1.5)NbC alloys, Acta Mater. 53 (2005) 4009–4018, https://doi.org/10.1016/j.actamat.2005.04.035.

[97] Z. Dong, U.E. Klotz, C. Leinenbach, A. Bergamini, C. Czaderski, M. Motavalli, A novel Fe-Mn-Si shape memory alloy with improved shape recovery properties by VC precipitation, Adv. Eng. Mater. 11 (2009) 40–44, https://doi.org/10.1002/adem.200800312.

[98] Y.H. Wen, L.R. Xiong, N. Li, W. Zhang, Remarkable improvement of shape memory effect in an Fe–Mn–Si–Cr–Ni–C alloy through controlling precipitation direction of Cr23C6, Mater. Sci. Eng. A 474 (2008) 60–63, https://doi.org/10.1016/j.msea.2007.05.043.

[99] M. Mohri, I. Ferretto, C. Leinenbach, D. Kim, D.G. Lignos, E. Ghafoori, Effect of thermomechanical treatment and microstructure on pseudo-elastic behavior of Fe–Mn–Si–Cr–Ni–(V, C) shape memory alloy, Mater. Sci. Eng. A 855 (2022), https://doi.org/10.1016/j.msea.2022.143917 143917.

[100] H. Khodaverdi, M. Mohri, E. Ghafoori, A.S. Ghorabaei, M. Nili-Ahmadabadi, Enhanced pseudoelasticity of an Fe-Mn-Si-based shape memory alloy by applying microstructural engineering through recrystallization and precipitation, J. Mater. Res. Technol. 21 (2022) 2999–3013, https://doi.org/10.1016/j.jmrt.2022.10.092.

[101] C. Leinenbach, H. Kramer, C. Bernhard, D. Eifler, Thermo-mechanical properties of an Fe–Mn–Si–Cr–Ni–VC shape memory alloy with low transformation temperature, Adv. Eng. Mater. 14 (2012) 62–67, https://doi.org/10.1002/adem.201100129.

[102] O. Matsumura, S. Furusako, T. Furukawa, H. Otsuka, Formation of surface texture and anisotropy of shape memory effect in an Fe-Mn-Si alloy, ISIJ Int. 36 (1996) 1103–1108, https://doi.org/10.2355/isijinternational.36.1103.

[103] A. Druker, C. Sobrero, H.-G. Brokmeier, J. Malarría, R. Bolmaro, Texture evolution during thermomechanical treatments in Fe–Mn–Si shape memory alloys, Mater. Sci. Eng. A 481–482 (2008) 578–581, https://doi.org/10.1016/j.msea.2006.10.214.

[104] T. Maruyama, H. Kubo, 12 - Ferrous (Fe-based) shape memory alloys (SMAs): properties, processing and applications, in: K. Yamauchi, I. Ohkata, K. Tsuchiya, S. Miyazaki (Eds.), Shape Memory and Superelastic Alloys, Woodhead Publishing, 2011, pp. 141–159, doi: 10.1533/9780857092625.2.141.

[105] S. Fu, H. Bei, Y. Chen, T.K. Liu, D. Yu, K. An, Deformation mechanisms and work-hardening behavior of transformation-induced plasticity high entropy alloys by in -situ neutron diffraction, Mater. Res. Lett. 6 (2018) 620–626, https://doi.org/10.1080/21663831.2018.1523239.

[106] A.A. Salem, S.R. Kalidindi, R.D. Doherty, Strain hardening regimes and microstructure evolution during large strain compression of high purity titanium, Scr. Mater. 46 (2002) 419–423, https://doi.org/10.1016/S1359-6462(02)00005-2.